

We are IntechOpen, the world's leading publisher of Open Access books Built by scientists, for scientists

6,900

Open access books available

185,000

International authors and editors

200M

Downloads

Our authors are among the

154

Countries delivered to

TOP 1%

most cited scientists

12.2%

Contributors from top 500 universities



WEB OF SCIENCE™

Selection of our books indexed in the Book Citation Index
in Web of Science™ Core Collection (BKCI)

Interested in publishing with us?
Contact book.department@intechopen.com

Numbers displayed above are based on latest data collected.
For more information visit www.intechopen.com



Processing and Characterization of Alumina / Chromium Carbide Ceramic Nanocomposite

Jow-Lay Huang and Pramoda K. Nayak
*National Cheng Kung University
Taiwan*

1. Introduction

Materials with nano-scale components as reinforcement phase are adding new dimensions to composite materials, thereby facilitating major improvement in functional and structural properties. Ceramic nanocomposites are the blends of different ceramic matrices with nanometer sized functional particles. The advantages of these nanocomposites include: improved mechanical properties, surface properties, decreased permeability to gases, water and hydrocarbons, higher thermal stability and heat distortion temperature, higher chemical resistance, smoother surface appearance and higher thermal conductivity. The incorporation of only a few percent of nano-sized particles makes great property changes and formerly unachievable property combinations possible.

The ceramic nanocomposites can be divided into three types; intragranular composite, intergranular composite and nano/nano composite (Niihara, 1991) according to their microstructures. In intra and intergranular nano-composite, the nano-sized particles are dispersed mainly within the matrix grains or at the grain boundaries of the matrix, respectively. The aim of these composites is to improve the mechanical properties such as hardness, fracture strength, toughness and also high temperature mechanical properties such as hardness, strength, creep and fatigue fracture resistances. On the other hand, nano/nano composites are composed of the dispersoids and matrix grains within the nanometer size. The primary purpose of this type of nano-composite is to add new functions such as machinability and super plasticity like metals to ceramics.

1.1 Synthesis of ceramic nanocomposite

Chemical Vapor Deposition (CVD) is a very preferable method to disperse the nano-sized second phases into the matrix grains or at the grain boundaries (Niihara & Hirai, 1986). $\text{Si}_3\text{N}_4/\text{TiN}$ was the first system prepared by CVD. However, the CVD process is not applicable to fabricate the large and complex shaped component for the mass production and also it is very expensive. Processing route is another technique to prepare ceramic nanocomposites. Following the initial work of (Niihara & Nakahira, 1988), several research groups have tried to synthesize the nanocomposites using processing route. There are several methods involve in processing route such as conventional powder processing (Borsa et al., 1999; Carroll et al., 1996; Niihara et al., 1989; Shapiro et al., 2009), sol-gel processing (Liu et al., 2006; Xu et al., 1994) and polymer processing (Borsa & Brook, 1995; Galusek et al.,

2007). The ceramic nanocomposites can be synthesized using microwave plasma (Vollath et al., 1997; Vollath & Szabó, 2006). In this process, the matrix material is coated with a layer of second phase material. The main advantage of this technique is that the reaction product does not form hard agglomerates because of the specific conditions during synthesis. Oxide and nitride based ceramic nanocomposites have been synthesized using microwave plasma technique (Vollath & Sickafus, 1993; Vollath & Sickafus, 1992). Recently developed sparked plasma synthesis (SPS) is an advanced technique for the synthesis of ceramic nanocomposites. The technique has a great advantage over conventional sintering technique, since the whole process can be complete in a few minutes, thus allowing nanosized grains of the sintering powder, and its crystal structure as well, to be retained in the sintered body. Various ceramic nanocomposites have been synthesized using SPS in literature (Dusza et al., 2009; Kumari et al., 2009; Trombini et al., 2009).

Furthermore, using all the above synthesis techniques for preparing ceramic nanocomposite, the nanoscaled reinforced particles are difficult to disperse uniformly on the micro-scale matrix particles. This problem is ascribed to the fact that nano-scale particles agglomerate easily due to the interaction between the particles. The agglomeration promote the generation of voids during the densification and microstructural in homogeneity. Kunii & Levenspiel, 1977 have recognized that a fluidized bed reactor can supply an environment with a uniform temperature and concentration of the coating precursor, which can provide the possibility of a good dispersion of reinforcing nano-particles in a matrix. A precursor vaporized at a low temperature is the major characteristic of the metal-organic chemical vapor deposition (MOCVD) process. The combination of conventional fluidized bed technology with standard chemical vapor deposition has been proven to be an effective method to deposit particles (Chen & Wei, 2002; Tsugeki et al., 1993).

1.2 Characteristics of ceramic nanocomposite

Microstructure and mechanical properties such as micro hardness, facture strength, and facture toughness are the main characteristics of ceramic nanocomposite materials. Apart from this, the nanocomposites also exhibit electro conductive, wear resistance, creep resistance and high temperature performance. One of the major characteristics and the greatest disadvantages of ceramics is their brittleness. Researchers have tried to compensate these disadvantages and to improve the strength of the nanocomposite. It has been observed that the facture strength of the brittle materials can only be improved by the increase in facture toughness or by reduction in critical flaw size (Davidge, 1979). Therefore, much effort has been invested in advanced processing technology to reduce the size and density of processing flaws (Lange, 1989). However, the design of tougher, flaw-tolerant ceramics is a more interesting approach for wider industrial applications. The facture toughness can be increased by incorporating various energy-dissipating components such as whiskers, platelets or particles into the ceramic microstructure (Becher, 1991; Lange, 1973). The reinforcements serve to deflect the crack or to provide bridging elements hindering further opening of the crack. Another concept is to incorporate metallic ligaments into the ceramic matrix (Sigl et al., 1988) to form crack bridging elements that absorb energy by plastic deformation.

1.3 Mechanisms of ceramic nanocomposite

In 1997, Sternitzke reviewed the modeling (strengthening and toughening mechanisms) of nanocomposites and divided the mechanisms into three groups; c-mechanism, K-

mechanism and grain boundary strengthening mechanism. The c-mechanism is based on the fact that the matrix becomes refined following the adding of nano-sized silicon carbide. A refinement of the grain size leads to smaller critical flaw size and higher strength. K-mechanism relates to R-curve behavior, crack deflection, and crack bowing during a crack extension. Ohji et al., 1998 proposed a particle-bridge mechanism, where there exists crackface shielding when nano-size particles bridge the crack surfaces. Crack deflection and crack bowing are related to the interactions of a crack front with second-phase inclusions which depend on the differences in the thermoelastic properties of the matrix and inclusions. Levin et al., 1995 and Sekino et al., 1997 explained that the strengthening mechanism of nanocomposites results from residual stresses around the second-phase particles, and matrix weakening and grain boundary strengthening produce the change of the fracture mode. Only nano-sized dispersed particles can improve the strength and the fracture toughness.

2. Alumina/chromium carbide nanocomposite

Alumina is one of the important materials in structural ceramic application because of its excellent mechanical properties, good chemical stability and high temperature characteristics (Ghate et al., 1975; Wang & Hsu, 1996). Its intrinsic brittleness and relatively poor reliability however, made the toughening of alumina ceramics an important and challenging area of research now days. The incorporation of secondary ceramic reinforcement phases (e.g. particulates, fibers, or platelets) has been proven to be an easy, safe and economically toughening technique for alumina ceramics (Chou & Green, 1992; Lio et al., 1989). There are several approaches by the researchers to toughen the alumina matrix with addition of different secondary phases. Among all the approaches, SiC reinforcement particles on Al_2O_3 composites mostly improve the mechanical properties (Anyia, 1999; Sternitzke, 1997). But the toughness enhancement is not significant for these composites. On the other hand, incorporating chromium carbide particles into Al_2O_3 matrix has been successfully achieved for toughening purposes (Fu et al., 1994; Huang et al., 2000; Lii et al., 1999). These aluminum oxide/chromium carbide composites demonstrate superior mechanical properties to those of matrix phase due to the high Young's modulus of chromium carbide and its outstanding ability to resist high temperature erosion at temperatures up to 1000°C . In addition, the good electrical conductivity of chromium carbide makes electrical discharge machining possible.

Besides second phase particles, solid solution strengthening is another mechanism for the Al_2O_3 matrix. Chromia (Cr_2O_3) has been used to improve the physical properties of Al_2O_3 (Bradt, 1967). As Cr_2O_3 has the same corundum crystal structure similar to Al_2O_3 , $\text{Al}_2\text{O}_3\text{-Cr}_2\text{O}_3$ can form substitutional solid solution in all ranges at high temperature. The addition of Cr_2O_3 was found to increase the hardness, tensile strength, and thermal shock resistance of Al_2O_3 .

This chapter will emphasize on the processing of Alumina/Chromium carbide ceramic matrix composite by metal oxide chemical vapor deposition (MOCVD) in fluidized bed and analysis of these composites using various characterization techniques. The synthesis parameters, microstructure and mechanical properties of the alumina/chromium carbide prepared by three different processes such as (i) Hot press sintering, (ii) Carbothermal reduction, and (iii) Spark plasma sintering, have been investigated and summarized in details in the following sections.

2.1 Experimental details

This section describes the raw powders, different types of synthesis procedures such as MOCVD, Hot press sintering (HP), Carbothermal reduction, Spark plasma sintering (SPS), and various characterization techniques such as X-ray diffraction (XRD), scanning electron microscopy (SEM), transmission electron microscopy (TEM), and energy dispersive spectroscopy (EDS), X-ray photoelectron spectroscopy (XPS) and electron energy loss spectroscopy (EELS) used in the current work. The flow chart showing the detailed experimental procedure is given in Fig.1.

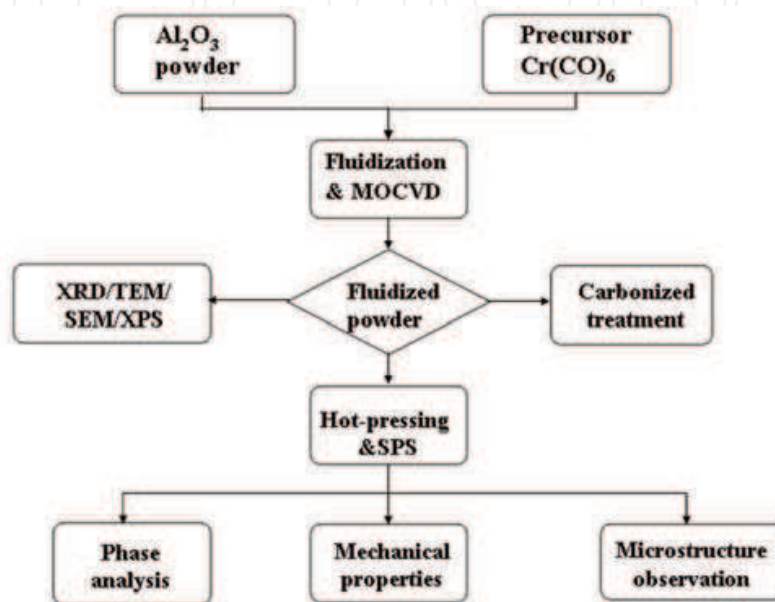


Fig. 1. Flow chart of the experimental procedure adopted in the current work.

2.1.1 Powder and sample preparation

Chromium hexacarbonyl ($\text{Cr}(\text{CO})_6$, 99%, Strem Chemicals Co., USA) was used as the precursor of chromium oxide in the MOCVD process. Aluminum oxide powder with the average particle size of about 0.2–0.4 μm (A16-SG, Alcoa, USA) was used as the matrix powder. A vaporized precursor carried by He gas (99.9% pure) was introduced into the fluidized bed reactor for the MOCVD process. Based on the results of Lander & Germer, 1947, the precursor container was kept at 75°C in a vacuum (10 torr) in the present experiment. To investigate the influence of the temperature on the product deposited on the fluidizing Al_2O_3 particles, the $\text{Cr}(\text{CO})_6$ vapor was decomposed in the fluidized chamber at 300 and 400 °C, respectively. The apparatus consisted of six main components: gas supply, MOCVD precursor, fluidized bed reactor, power supply, temperature controller, cold trap and vacuum system, as shown schematically in Fig. 2. (Lin et al., 2006a). The pressure in the chamber was measured with a pressure meter. A rotary vacuum pump was set up with a cold trapping system. The temperature controllers (TC) were connected to a heating system that controlled the temperature of the fluidized reactor and precursor container.

2.1.2 Characterization of the fluidized powder

The fluidized powders were analyzed by x-ray diffraction (XRD; Rigaku D/MaxII, Japan), and transmission electron microscopy (TEM; Hitachi FE-2000, Japan) equipped with energy

dispersive x-ray spectroscopy (EDS; UK). X-ray photoelectron spectroscopy (XPS; VG Scientific 210, UK) was used to determine the coating phases by binding energy. A Brunauer-Emmett-Teller (BET) instrument Micromeritics Gemini 2360, USA) was used to measure the specific surface area by nitrogen adsorption, and C/O analyzer (LECO CS-244, USA) was used to measure the carbon content of coated powder by a combustion method. Fig. 3 shows the XRD patterns of decomposed $\text{Cr}(\text{CO})_6$ prepared in fluidized bed at 300°C and 400°C . It is observed that at 300°C , the powder is completely amorphous in nature, whereas at 400°C , the powder consists of Cr_2O_3 along with CrC_{1-x} phase (Lin et al., 2006b).

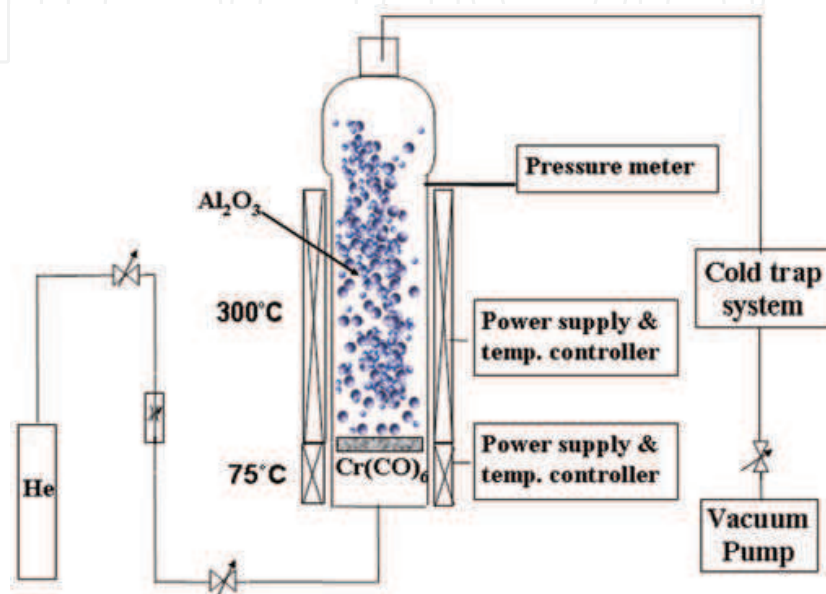


Fig. 2. Schematic diagram of MOCVD and fluidized bed.

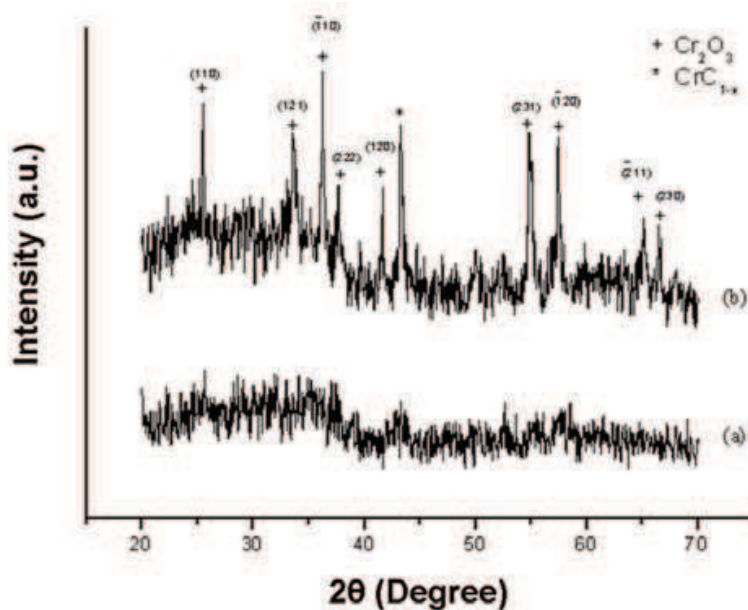


Fig. 3. XRD pattern of decomposed $\text{Cr}(\text{CO})_6$ prepared in fluidized bed at (a) 300°C (b) 400°C .

The pyrolysis of precursor $\text{Cr}(\text{CO})_6$ at 300°C results the formation of Cr_2O_3 , C-Cr and C-C bonds observed from XPS spectra (Fig. 4). This figure displays the XPS spectra of the Cr $2p$ and C $1s$ regions of the as-deposited powder prepared at 300°C . Fig. 4a shows two peaks corresponding to the spin-orbit splitting $2p_{1/2}$ (right) and $2p_{3/2}$ (left) of Cr with bonding energies of 586.3 and 576.6 eV, respectively. The band shift of these two peaks is 9.7 eV, which is in good agreement with previously reported data (Wagner et al., 1979) and confirms the existence of Cr_2O_3 particles in the as-deposited powder. The XPS spectra of the C $1s$ regions in Fig. 4b provide the evidence for which at least two forms of carbon in the as-deposited powder exist. One is free carbon (C-C) at 284.6 eV, and the other carbon bonded to chromium atoms (C-Cr) at 283.5 eV.

The decomposed precursor deposits uniformly over Al_2O_3 and the deposited nano particles ($\sim 30\text{ nm}$) are shown in the TEM micrograph (Fig. 5a). The insert shows the TEM pattern of the deposited nano particles, which is amorphous in nature. From the EDS spectrum shown in Fig. 5b, it is confirmed that the nanoparticles consist of mostly Cr and O along with small amount of C. The presence of Cu is the contribution from Cu grid.

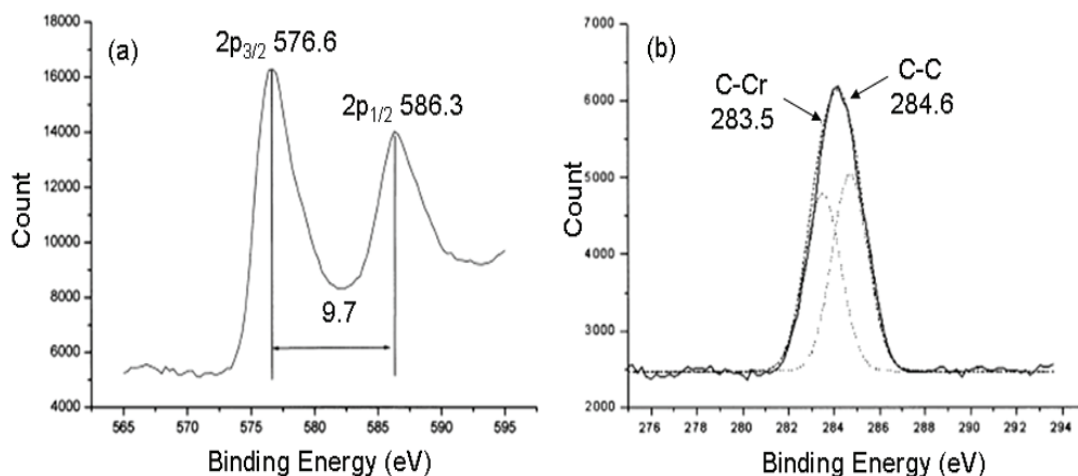


Fig. 4. X-ray photoelectron spectra of the (a) Cr $2p$ regions and (b) C $1s$ regions of as deposited composite powders prepared at 300°C in fluidized bed.

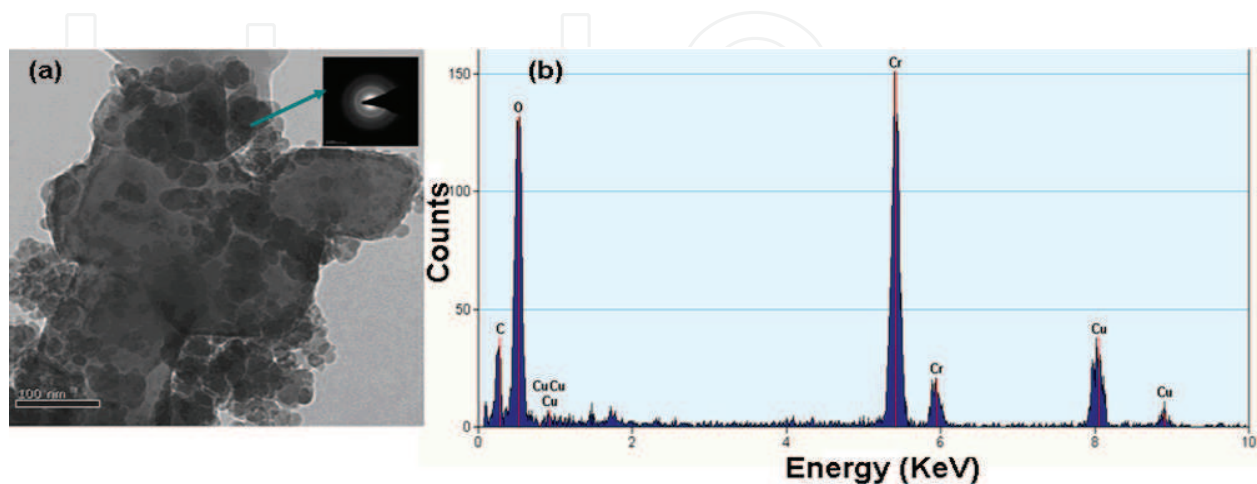


Fig. 5. TEM micrographs of (a) nanoparticles deposited on alumina particle (b) EDS spectrum of the coating particle.

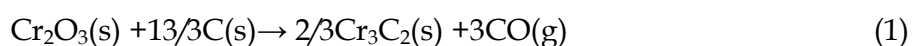
Table 1 shows the carbon content of the samples prepared at different fluidized temperature. The carbon content is 0.75 and 0.23% for the samples fluidized at 300 and 400°C, respectively. It indicates that the as-deposited amorphous powder prepared at 300 °C has more carbon content than the crystalline powders prepared at 400°C. This was probably because of the amorphous powder has specific surface area (25.5m²/g) larger than the crystalline powder (11.2 m²/g).

Specimen	Fabricated in Fluidized reactor	Carbon content (%)	BET surface area (m ² /g)
1	300° C, 2h	0.75	25.5
2	400° C, 2h	0.23	11.2

Table 1. Specific surface area and carbon content of specimens

3. Carbothermal treatment of Cr₂O₃ particles dispersed on Al₂O₃ particles

The carbothermal treatment of the prepared Cr₂O₃/Al₂O₃ powders was first performed in a graphite furnace at a variety of temperatures from 700 to 1150 °C in a vacuum condition (10⁻³ Torr) for 2h. Fig. 6. shows the XRD patterns of the fluidizing powders treated from 700 to 1150 °C in the graphite furnace for 2 h. The Cr₂O₃ peaks seen in the XRD patterns clearly indicate that the amorphous Cr₂O₃ has crystallized, but does not carbonize at temperatures under 1000 °C. As reported by Bouzy et al., 1993 and Bewilogua et al., 1988, an annealing treatment causes a transformation of the metastable carbide CrC_{1-x} into the stable carbide phase Cr₃C₂. Here, Cr₃C₂ peaks are not observed in the XRD patterns shown in Fig. 6a-6d, consequently, suggesting that the CrC_{1-x} content of the decomposed Cr (CO)₆ is too little to be found in XRD patterns. According to the XRD pattern shown in Fig. 6e, Cr₂O₃ reacts with carbon and transforms into Cr₃C₂ when the treatment temperature is 1150 °C. This carbothermal reaction process (Storms, 1967) can be shown as the following equation:



3.1 The formations of Cr-carbide/Al₂O₃ nanocomposite and Cr₂O₃/Al₂O₃ solid solution

After carbothermal treatment, the fluidized powders undergone hot pressed sintering at 1400° C. For this process, the 200 mesh fluidized powder was first die-pressed, and then put into a BN-coated graphite die and hot-pressed at a pressure of 25MPa in a HP furnace (High-multi 5000, Fujidempa Kogyo Co., Ltd., Japan) at 1400°C under vacuum (5×10⁻⁴ torr). The detailed sintering conditions of the different samples are listed in Table 2.

Samples	Sintering powders	Sintering conditions
ALO	Pure alumina powder	1400°C/1h, pressure 25 MPa
Sample 1	Composite powders fluidized at 300° C for 1 h	1000°C/1h, 1400°C/1h, 25 MPa
Sample 2	-do-	1150°C/1h, 1400°C/1h, 25 MPa
Sample 3	-do-	1400°C/1h, pressure 25 MPa

Table 2. Sintering conditions of hot pressed samples

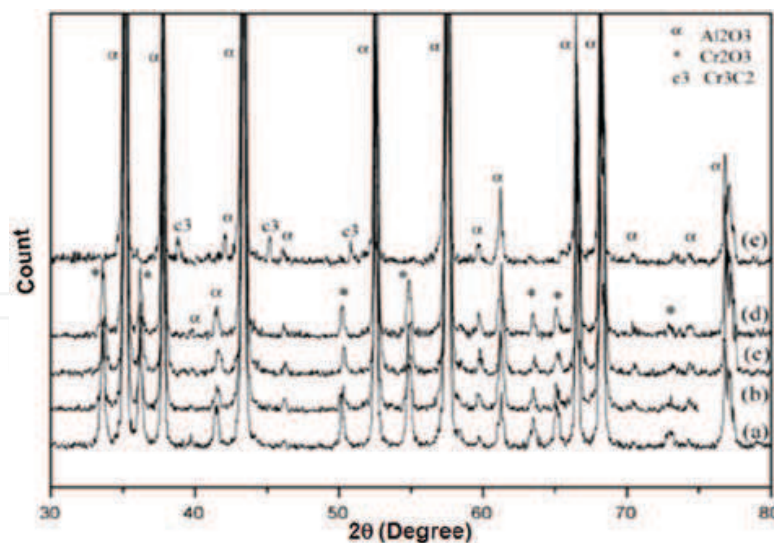


Fig. 6. XRD patterns of the powder thermally treated at a variety of temperatures: (a) 700 °C, (b) 800 °C, (c) 900 °C, (d) 1000 °C, and (e) 1150 °C in a vacuum in a graphite furnace for 2 h for the fluidized powders prepared in the fluidized bed.

Fig. 7 shows the XRD patterns of the samples thermally treated under different conditions. The Si peaks shown in the XRD pattern were used for calibration. First, Fig. 7a and 7b indicate that the Al_2O_3 peaks for sample 1 shifted to lower angles than those for Al_2O_3 . For pure Al_2O_3 , the pure alumina powder was hot pressed at 1400 °C, while for sample 1, the fluidized powder was pre-sintered at 1000 °C before the hot pressing at 1400 °C. During the pre-sintering at 1000 °C, most of the Cr_2O_3 reacted with Al_2O_3 to form an Al_2O_3 - Cr_2O_3 Solid solution and thus the Al_2O_3 peaks shifted to lower angles in the XRD pattern. Furthermore, the color of the pieces is dark red (Nassau, 1983) as observed in sample 1, due to the $(\text{Al}, \text{Cr})_2\text{O}_3$ solid solution reaction product. Secondly, a comparison with the peaks of Al_2O_3 reveals that the Al_2O_3 diffraction peaks of sample 2, as shown in Fig. 7c, shift to lower angles, occurring simultaneously with the peaks of Cr_3C_2 . Consequently, besides forming a solid solution, some of the Cr_2O_3 reacts with carbon as equation (1) to form chromium carbide Cr_3C_2 when the powders have been pre-sintered at 1150 °C (Lin et al., 2007). Finally, Fig. 7d shows the XRD patterns of sample 3, which is similar to the results of sample 2. In addition to forming a solid solution, some of the Cr_2O_3 was also carbonized. However, it transformed into mixed phases of Cr_3C_2 and Cr_7C_3 when the fluidized powders were hot pressed at 1400 °C. Berger et al., 2001 reports that Cr_7C_3 is formed at an elevated temperature (>1150 °C). Moreover, the TG/DTA results of our paper (Lin et al., 2005) also indicate that the generation temperature of Cr_7C_3 is about 1170 °C. This carbothermal reaction process (Bradt, 1967) can be shown as reaction (2). Consequently, not only Cr_3C_2 , but also Cr_7C_3 is formed in sample 3, hot pressed at 1400 °C.

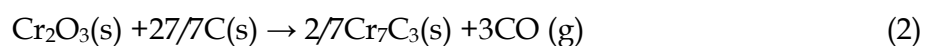


Fig. 8a shows the SEM micrograph of pure Al_2O_3 and 8b is the High Angle Annular Dark Field scanning transmission electron microscopy (HAADF STEM) image of sample 1, showing almost all the Cr^{3+} replaced the Al^{3+} and formed an Al_2O_3 - Cr_2O_3 solid solution. According to Bondioli et al., 2000, at temperatures of over 1000 °C the complete ranges of substitutional solid solutions are obtained. Fig. 8c and 8d are the HAADF STEM images of samples 2 and 3, respectively, showing that in addition to forming a solid solution,

nanosized chromium carbide particles also disperse uniformly in the alumina matrix. Comparing the HAADF STEM images of samples, sample 2 has smaller alumina grain size ($0.7\mu\text{m}$) than others (sample 1: $1.5\mu\text{m}$, sample 3: $0.9\mu\text{m}$.) This is because it has much nanosized particles on the Al_2O_3 grain boundaries, which effectively inhibit the grain growth. The volume percentages of the reinforced particles showing in Fig. 8c and 8d are 4.5 and 1.5 vol%, respectively. Conversely, the Al_2O_3 grains of sample 1 have a larger growth size as a result of the diffusion of Cr atoms inducing grain boundary migration (DIGM) (Han et al., 1995). The drive force for the migration is believed to rise from the coherency strain in the Cr_2O_3 diffusion zone in front of the migrating grain boundaries.

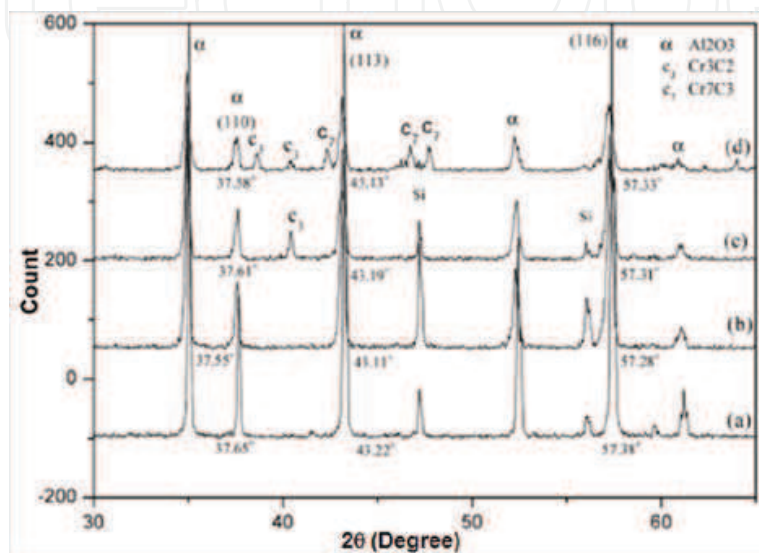


Fig. 7. XRD patterns of hot pressed samples: (a) AlO , (b) sample 1, (c) sample 2, and (d) sample 3.

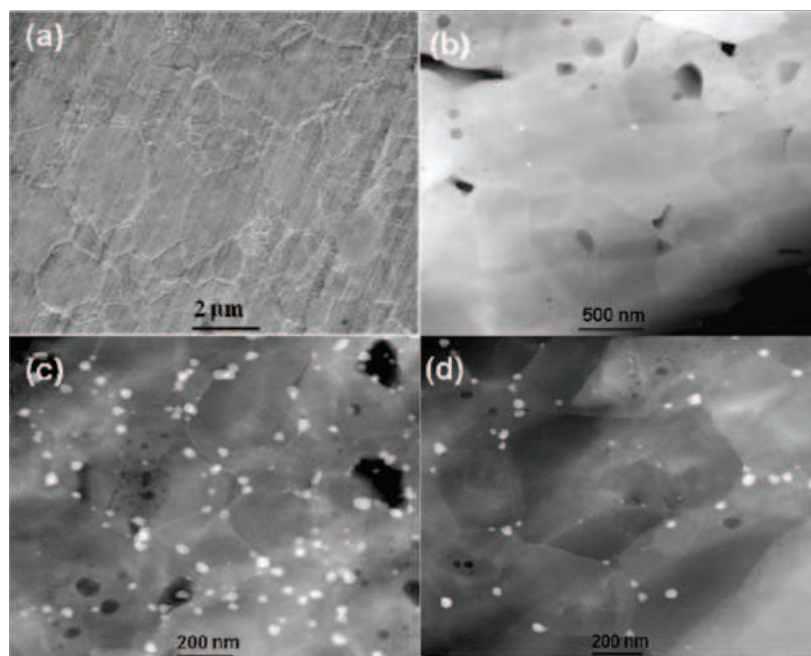


Fig. 8. SEM micrograph of (a) pure Al_2O_3 ; HAADF STEM micrographs of samples: (b) sample 1: $\text{Al}_2\text{O}_3\text{-Cr}_2\text{O}_3$, (c) sample 2: $\text{Al}_2\text{O}_3\text{-Cr}_3\text{C}_2$ and (d) sample 3: $\text{Al}_2\text{O}_3\text{-Cr}_7\text{C}_3$.

There are two HRTEM micrographs of interfaces shown in Fig. 9. One is the interface between the Cr_3C_2 and Al_2O_3 and the other is the interface between Cr_7C_3 and Al_2O_3 . The interface between Al_2O_3 and Cr_3C_2 is non-coherent, as shown in Fig. 9a. The smaller illustrations in Fig. 9a show Al_2O_3 with hexagonal and Cr_3C_2 with orthorhombic structure. The lattice spacing of the Al_2O_3 ($\bar{1} 0 1 4$) is 0.255 nm and that of the Cr_3C_2 (0 0 2) is 0.115 nm. The spacing difference between these two planes is large. However, the interface between Al_2O_3 and Cr_7C_3 is semi-coherent, as shown in Fig. 9b. Structures of both Al_2O_3 and Cr_7C_3 are hexagonal. The lattice spacing of the Al_2O_3 plane ($\bar{1} 1 0 2$) and Cr_7C_3 plane ($2 \bar{2} 0 1$) are 0.349 and 0.360 nm, respectively. There is little difference between the lattice spacing of these two hexagonal planes.

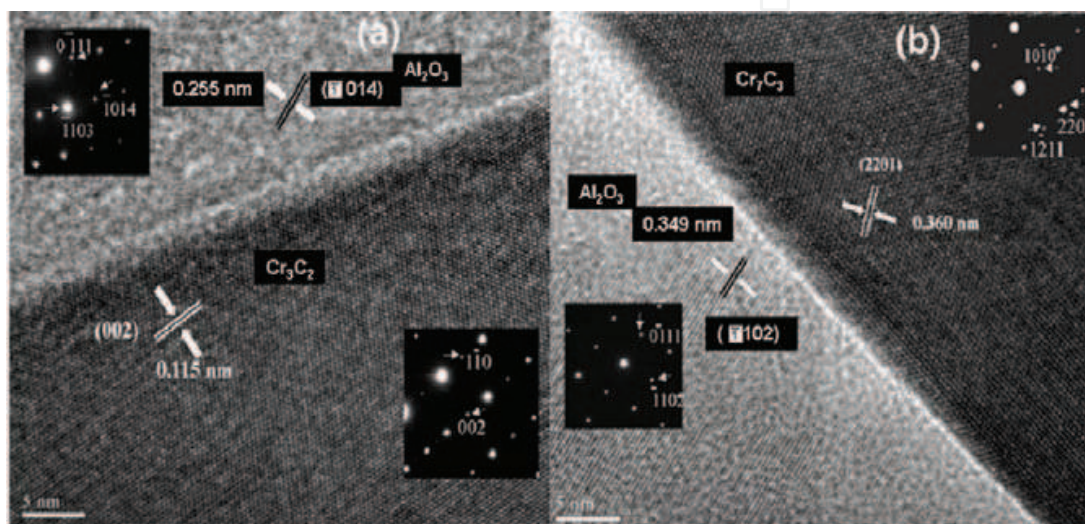


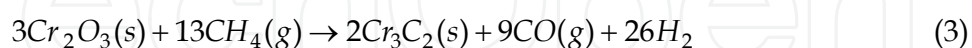
Fig. 9. Lattice images of the interfaces (a) between Cr_3C_2 and Al_2O_3 , and (b) between Cr_7C_3 and Al_2O_3 .

3.2 Carbothermal reduction of Cr_2O_3 using methane as carbonization source

The conventional route for Cr_3C_2 composite synthesis mainly involves the reduction of chromium oxide by methane gas (Anacleto & Ostrovski, 2004). However, besides the three stable chromium carbides, Cr_3C_2 , Cr_7C_3 , and Cr_{23}C_6 , several metastable carbides such as Cr_3C , CrC_{1-y} , Cr_5C_2 and $\text{Cr}_3\text{C}_{2-x}$ also have been reported, which emanate during different preparation methods and for different Cr/C contents (Bewilogua et al., 1988; Bouzy et al., 1993; Inoue & Masumoto, 1979). Lerch & Rousset, 1994 indicated that the $\text{CrO}_{1.9}$ with high surface area (200–350 m^2/g) reduced at 700 °C in an atmosphere of methane and hydrogen mixture leading to the formation of stable Cr_3C_2 and metastable $\text{Cr}_3\text{C}_{2-x}$. The metastable $\text{Cr}_3\text{C}_{2-x}$ powder was also prepared by Loubière et al., 1995 & 1996 using $\text{CH}_4\text{-H}_2$ atmosphere from the carburization of metastable chromium oxide. The metastable $\text{Cr}_3\text{C}_{2-x}$ is a Re_3B -type structure, readily formed by carburization of high specific surface area chromium oxide and usually co-existent with Cr_2O_3 , Cr_3C_2 and free carbon.

In the previous sections, we have discussed the synthesis of $\text{Cr}_2\text{O}_3/\text{Al}_2\text{O}_3$ composite powders by the decomposition of chromium hexacarbonyl in a fluidized bed. This was followed by the hot-pressing of the composite powders in a graphite mode eventually leading to its transformation into a $\text{Cr}_3\text{C}_2/\text{Al}_2\text{O}_3$ nanocomposite. One of the major drawbacks in this synthesis process was the formation of undesirable $\text{Al}_2\text{O}_3\text{-Cr}_2\text{O}_3$ solid

solution at a high temperature, which leads to abnormal grain growth of the Al_2O_3 matrix and eventually decreased the desired Cr_3C_2 contents in the composite. In order to carburize the chromium oxide completely, a new approach is reported by using the carburization process of nanosized chromium oxide formed from a metal-organic chromium hexacarbonyl precursor in a carburizing mixture of CH_4/H_2 gas. For this process, the as received powder after fluidization was carburized in an alumina tube furnace in the presence of a methane-hydrogen mixture (1:9) at 700–850 °C for 5 h. The H_2 restrain the CH_4 to decompose fast and using CH_4 as carbon source, the carbothermal reduction reaction becomes



Where, $\Delta G = 262564.44 - 236.79T$ (Cal) and ($T > 841^\circ \text{C}$)

Fig. 10 shows the XRD patterns of the decomposed powder carburized at 700–850 °C for 5 h in $\text{CH}_4\text{-H}_2$ gas. At the carburization temperature of 700 °C, the pattern displays sharp peaks that index with the Cr_2O_3 phase. At the increased carburization temperature of 750 °C, the intensity of Cr_2O_3 peaks decreases significantly accompanied by some incipient low intensity peaks which could be indexed with metastable $\text{Cr}_3\text{C}_{2-x}$. When the temperature reaches to 800 °C, the Cr_2O_3 phase disappears, concomitant with a complete transformation to the $\text{Cr}_3\text{C}_{2-x}$ phase. Further increase of the carburization temperature to 850 °C, leads to the formation of the stable Cr_3C_2 phase along with a small amount of $\text{Cr}_3\text{C}_{2-x}$ metastable phase (Wang et al., 2010).

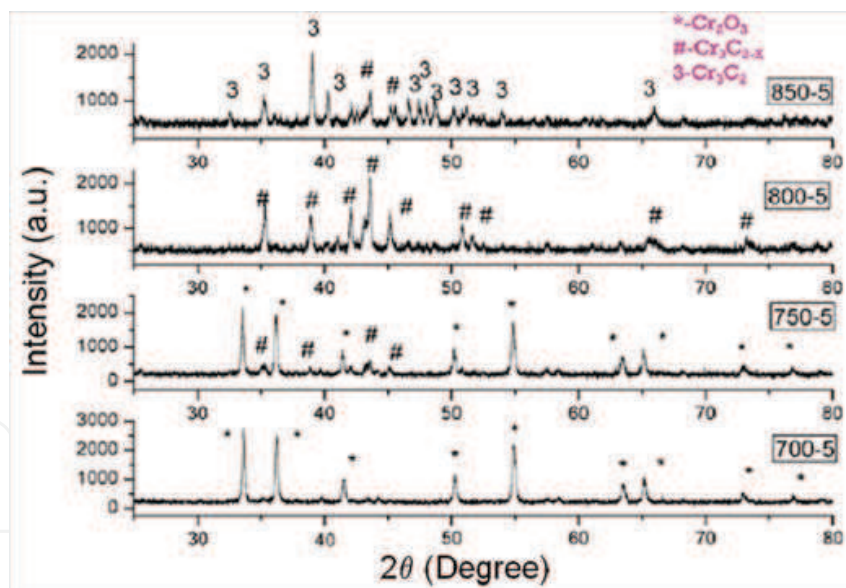


Fig. 10. XRD patterns of the decomposed precursor at different temperature.

For further validation of carburization process, the powders for different carburization temperature were characterized by TEM. Fig. 11a shows the TEM micrograph of the powder treated at 700 °C, where the particle size is found to be around 40 nm. The diffraction pattern verifies its phase for the chromium oxide Cr_2O_3 , (rhombohedral structure). The high resolution image shows a clear atomic image inside the powder. A thin amorphous layer is visible in a different contrast outside the boundary surface. This can be attributed to the adsorption of carbon deposit on the powder surface. Fig. 11b shows the TEM and HRTEM

of powdered samples carburized at 800 °C for 5 h. The spherical shape has transformed to faceted irregular grain. The diffraction pattern confirms that the phase is attributed to metastable $\text{Cr}_3\text{C}_{2-x}$, which is in accordance with the XRD result. The HRTEM image shows that there are several carbon nanofilms formed around the surface of the powder surface. The Fast Fourier transform (FFT) pattern of these layers, shows two obvious halo spots that are attributed to the graphene structure of carbon nanofilms. The TEM micrographs of the powders, carburized at 850 °C, show that the powder is encapsulated by layers of graphene, as shown in Fig. 11c. The diffraction pattern verifies that the powder comprises the stable Cr_3C_2 phase.

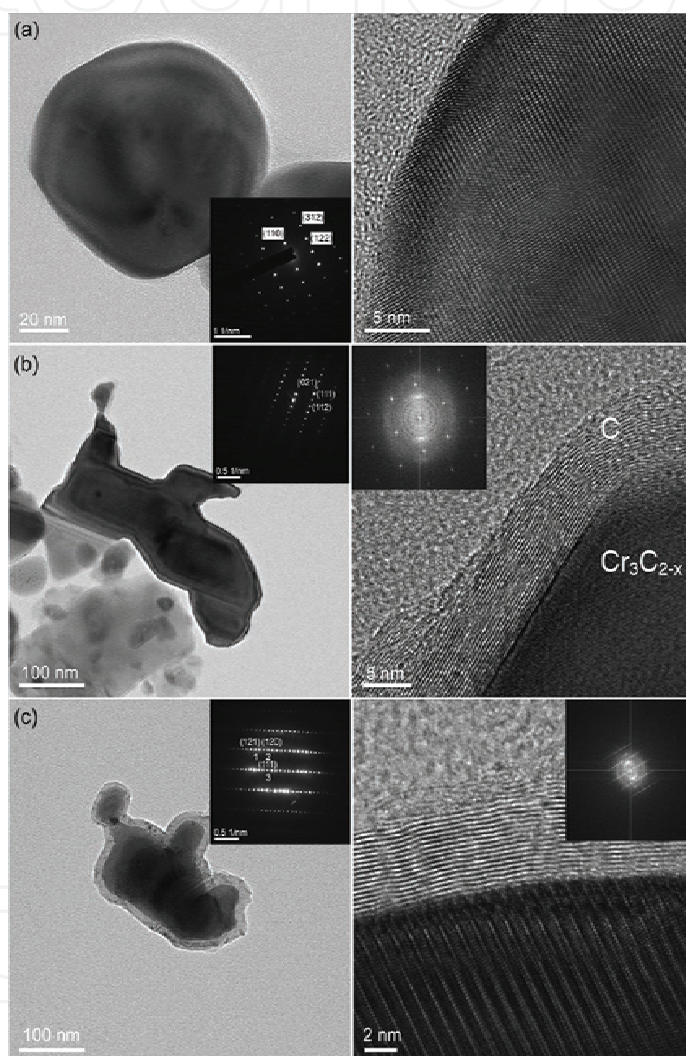


Fig. 11. TEM image of decomposed powder after the carbonized treatment (a) 700 °C/5 h; (b) 800 °C/5 h; (c) 850 °C/5 h.

The phase transformation from Cr_2O_3 to Cr_3C_2 via an intermediate state $\text{Cr}_3\text{C}_{2-x}$ has been identified using electron-energy loss spectroscopy (EELS). The EELS of prepared samples were characterized by field emission gun scanning transmission electron microscopy (FEG-STEM) equipped with energy dispersive X-ray detector (EDS) and energy filter (Gatan). Fig.12 shows the EELS spectra of Cr L edge for the sample of the decomposed precursor and the samples carbonized at 800°C and 850°C. The chromium L edges have features comprising

two sharp L_2 and L_3 , known as “white lines” (Lozzi et al., 1991) and a continuum background following the edge. The sharp double peaks are due to transitions from the $2p^{1/2}$ and $2p^{3/2}$ core levels towards $3d$ states above E_f . The sharp peaks of L_2 and L_3 at threshold are due to the transitions from the $2p^{1/2}$ core levels to $3d^{3/2}$ states and the $2p^{3/2}$ core levels to $3d^{3/2} 3d^{5/2}$, respectively. The L_3/L_2 white line ratio is correlated to the electron occupancy and spin pairing in $3d$ band. The variations of the ratio are due to the interaction between chromium and surrounding atoms. A change of the L_2 , L_3 edge intensities in the samples indicates a variation of the d holes because the edge intensity is proportional to the number of the empty final states available. The ratio of L_3/L_2 of sample shown in Fig. 12a is higher than that of carbonized samples. According to the results of Arévalo-López & Alario-Franco, 2009, the ratio of L_3/L_2 for the Cr_2O_3 is about 1.6 and from the report of Fan et al., 1999, the ratio of L_3/L_2 for the Chromium carbide is about 1. A comparison between Fig. 12b and 12c shows L_3 edge of the sample carbonized at $850^\circ C$ is $577.72 eV$, while that of sample carbonized at $800^\circ C$ is $575.42 eV$. The shift in energy ($2.3 eV$) is called the chemical shift. This result is due to the transformation from the metastable carbide to stable carbide, because the EELS represent the difference in energy between a core-level initial state and the lowest energy final state of an excited electron. But the energy loss close to $577.72 eV$ for the decomposed precursor (Daulton et al., 2002), which consists of Cr_2O_3 is same as the sample carbonized at $850^\circ C$. It is observed that there is no chemical shift between this two species because Cr_2O_3 and Cr_3C_2 are both chemically stable compounds.

The π electron formed sp^2 bonding observed from the EELS spectra of C K edges as shown in Fig. 12. The peak of sp^2 bonding is sharper when the carbonized temperature increases from $800^\circ C$ to $850^\circ C$. The sharpening of sp^2 peak is attributed to the formation of graphite like carbon according to Fan et al., 1999. In Cr_3C_2 , C is graphite like rather than diamond like, which comprising of sp^3 bonded carbon atoms. For the as decomposed precursor, the content of carbon was little and formed amorphous phase. More carbon produced from the pyrolysis of methane coated on the Cr_2O_3 surface and then formed graphite phase and metastable carbide of Cr_3C_{2-x} , when the sample was treated at $800^\circ C$ for 5 hours. The increase of treated temperature to $850^\circ C$, enhanced the process of carbonizing reaction leading to more graphite formation followed by transformation of metastable Cr_3C_{2-x} to stable carbide of Cr_3C_2 (Lin et al., 2011).

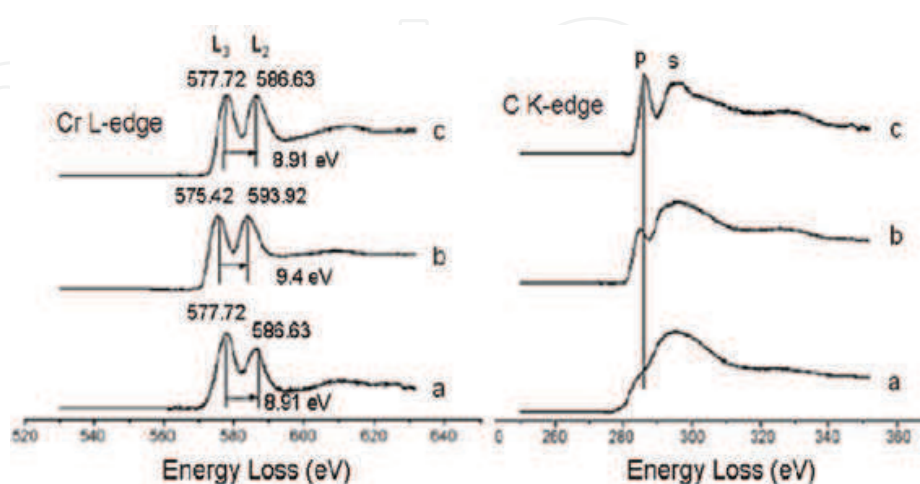


Fig. 12. EELS of Cr L edges & C K edges : (a) decomposed precursor, (b) carbonized at $800^\circ C/5 h$ (Cr_3C_{2-x}), and (c) carbonized at $850^\circ C/5 h$ (Cr_3C_2).

Based on these above results, one could hypothesize the following phase transformation steps: In the first step, the methane decomposes to elemental carbon and hydrogen (Muradov, 1998 & 2001). The carbon reacts with the Cr_2O_3 at temperatures higher than 800°C , and produce partial Cr_3C_2 phase and $\text{CO}_{(g)}$. The $\text{CO}_{(g)}$ can also carburize the Cr_2O_3 further. There are three kinds of carbon sources in the system viz. free carbon from the decomposition of methane, CO from above reaction and C-C bonding from the precursor. Finally, the unreacted redundant carbon sources would deposit on the surface of the powder as the lamellar graphene. The graphene deposited during the carburization has an important role for the formation of meta-stable $\text{Cr}_3\text{C}_{2-x}$ and stable Cr_3C_2 . Initially, carbon gets absorb on the surface of chromium oxide at low temperature. As the temperature rises, substantial amount of carbon is available, leading to metastable chromium carbide. Finally, as the temperature increases further, the redundant carbon forms the graphene layers. Further thickening of the graphene films, generates a mechanical stress (Loubière et al., 1996) which assists the transformation of meta-stable $\text{Cr}_3\text{C}_{2-x}$ state to stable Cr_3C_2 phase.

3.3 Microstructure and mechanical properties of $\text{Cr}_3\text{C}_2/\text{Al}_2\text{O}_3$ nanocomposites

As discussed in the previous sections, the carbonization treatment of initial powders without using methane as the carbon source leads to the formation of $(\text{Cr}_3\text{C}_2, \text{Cr}_7\text{C}_3)/\text{Al}_2\text{O}_3$ nanocomposites, where as carbonization using methane as carbon source leads to $\text{Cr}_3\text{C}_2/\text{Al}_2\text{O}_3$ nanocomposites, which is the desired material. In order to improve the mechanical properties of these $\text{Cr}_3\text{C}_2/\text{Al}_2\text{O}_3$ nanocomposites, the carbonized powders were undergone hot-press sintering at 1400°C for 1 hr in vacuum.

Fig. 13 shows the SEM micrographs of monolithic Al_2O_3 and $\text{Cr}_3\text{C}_2/\text{Al}_2\text{O}_3$ nanocomposites carbonized at different temperatures for 5 hours and hot-pressed at 1400°C for 1 hr in vacuum. One can see that there is abnormal grain growth of Al_2O_3 shown in Fig. 13a. In case of $\text{Cr}_3\text{C}_2/\text{Al}_2\text{O}_3$ nanocomposite, the dispersion secondary phase, Cr_3C_2 is uniform (Fig. 13b) and the abnormal grain growth has been inhibited. The grain size distribution of monolithic Al_2O_3 and $\text{Cr}_3\text{C}_2/\text{Al}_2\text{O}_3$ nanocomposites has been shown in Fig. 14. The nanocomposite exhibits low grain size than that of pure alumina. It implies that addition of Cr_3C_2 decreases the grain size and inhibits the growth of alumina matrix.

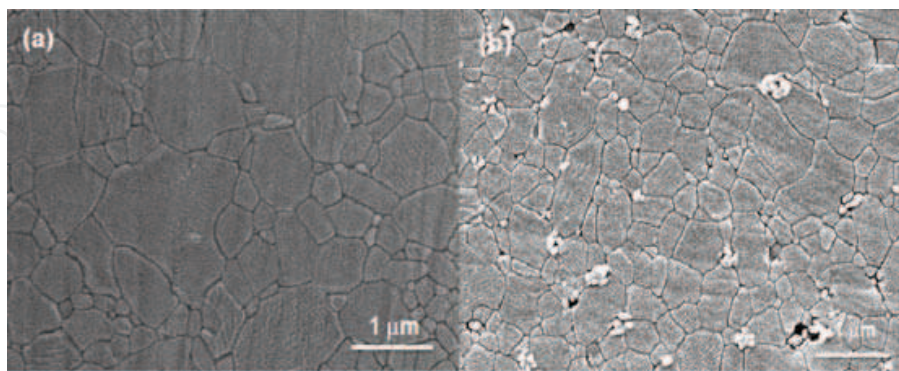


Fig. 13. SEM micrographs of (a) monolithic Al_2O_3 and (b) $\text{Cr}_3\text{C}_2/\text{Al}_2\text{O}_3$ nanocomposites by carbonized at different temperatures for 5 hours and hot-pressed at 1400°C for 1 hr in vacuum.

The TEM micrograph of $\text{Cr}_3\text{C}_2/\text{Al}_2\text{O}_3$ nanocomposites shown in Fig.15 illustrates two types of inclusion of Cr_3C_2 onto the Al_2O_3 matrix i.e. inter-type inclusion (Fig.15a) and intra-type inclusion (Fig. 15b). Fig. 16 shows the SEM micrographs of the fracture surface of monolithic

Al_2O_3 and $\text{Cr}_3\text{C}_2/\text{Al}_2\text{O}_3$ nanocomposites under the same carbonization condition. The fracture surface of pure alumina is intergranular in nature, where as transgranular fracture surface is observed in $\text{Cr}_3\text{C}_2/\text{Al}_2\text{O}_3$ nanocomposites.

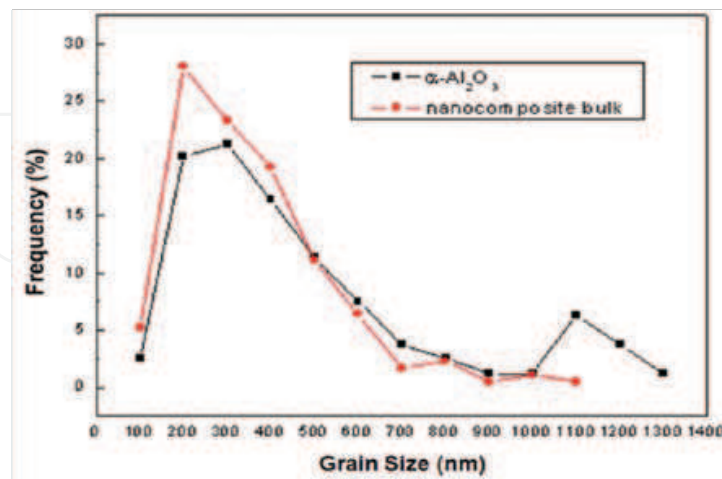


Fig. 14. Grain size distribution of (a) monolithic Al_2O_3 and (b) $\text{Cr}_3\text{C}_2/\text{Al}_2\text{O}_3$ nanocomposites prepared by carbonization at different temperatures for 5 hours followed by hot-press sintering at 1400°C for 1 hr in vacuum.

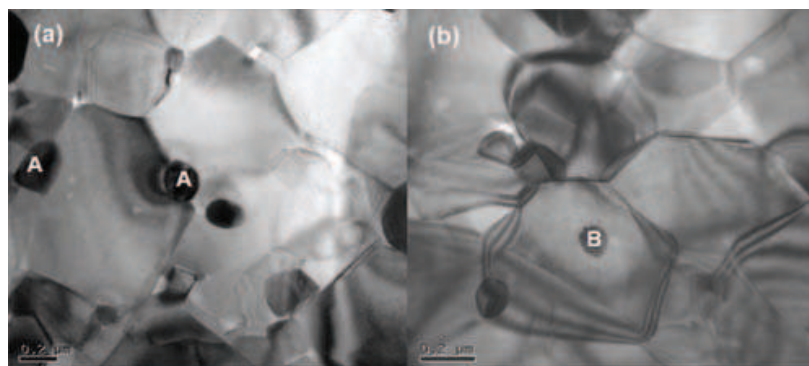


Fig. 15. TEM micrographs of $\text{Cr}_3\text{C}_2/\text{Al}_2\text{O}_3$ nanocomposites (a) inter-type inclusion in A (b) intra-type inclusion in B.

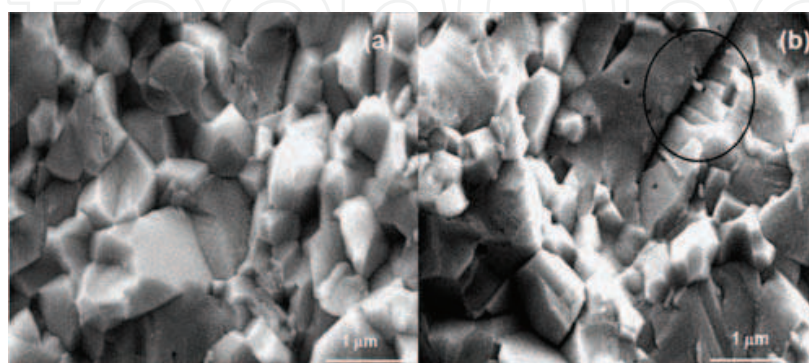


Fig. 16. SEM micrographs of the fracture surface (a) monolithic Al_2O_3 and (b) $\text{Cr}_3\text{C}_2/\text{Al}_2\text{O}_3$ nanocomposites prepared by carbonized at different temperatures for 5 hours hot-pressed at 1400°C for 1 hr in vacuum.

The basic mechanical properties such as hardness, fracture strength and toughness of pure alumina as well as of this nanocomposite have been analyzed and mentioned in table 3. The fracture strength was determined by 4-point bending (Shimadzu AG-IS 100KN, Japan). The toughness was measured by Single-Edge-Pre-cracked Beam (SEPB). A precrack with depth of 0.254mm was conducted in the center of sample by a diamond cutter with a thickness of 0.15mm. It is observed that the nanocomposite exhibits improved hardness, fracture strength and fracture toughness in comparison to monolithic alumina. The relationship between the microstructure and improved mechanical property has been investigated and described below.

Specimen	Hardness	Strength (4 pt-bending)	Toughness (Indentation Fracture method)
Al ₂ O ₃	18.4 GPa	375 MPa	4.0 MPa.m ^{1/2}
Cr ₃ C ₂ /Al ₂ O ₃	19.8 GPa	520 MPa	5.5 MPa.m ^{1/2}

Table 3. Mechanical property measurements on monolithic Al₂O₃ and Cr₃C₂/Al₂O₃ nanocomposites

The nanocomposites consisting of Cr₃C₂ particles dispersed within Al₂O₃ matrix grains, result in the generation of thermally induced residual stresses after hot-pressed sintering at 1400°C. The mismatch in thermal expansion coefficient between the matrix (α -Al₂O₃= 8.4*10⁻⁶/ °C), and the dispersed particles (Cr₃C₂=11.2*10⁻⁶/ °C) yields highly localized residual stresses around the particles. These stresses reduce quickly as distance from the boundary increases because of the nano-sized particles, which can generate only small defects such as dislocations shown in Fig. 17a in close vicinity to the particles (Awaji et al., 2002; Choi & Awaji, 2005). In the monolithic alumina, crack propagates along with the grain boundaries due to the existence of defects and the compress residual stresses resulting from anisotropic thermal expansion, Young's modulus along the crystal axes, and crystallographic misorientation across the grain boundaries. The fracture toughness of grain boundaries is usually lower than that within the grains. However, in nanocomposites, the dislocations around the Cr₃C₂ particles release residual stresses in the Al₂O₃ matrix. Consequently, the defect size along the grain boundaries is reduced. Also, the dislocations serve as origins of small stress concentrations, and create nano-cracks around the propagating crack tip. These nano-cracks slightly reduce the strength of the alumina matrix, while reduction of both the residual stresses along the grain boundaries and the strength in the matrix lead to a change in the fracture mode from that of the intergranular fracture in monolithic alumina to that of transgranular fracture in nanocomposites, as shown in Fig. 16b. In addition, due to the effect of nano-cracking, the step-wise fracture surface rather than a planar cleavage plane is observed in the nanocomposites (Choi et al., 2004), as shown in Fig. 17b. The reinforcement of the Cr₃C₂ particles, small grain size of Al₂O₃ matrix and reduction of both the defect size along the grain boundaries and the tensile residual stresses in the matrix grains by dislocations result in improvement of the strength of nanocomposites.

In the case of Cr₃C₂-Al₂O₃ solid solution described in the previous section, the Cr³⁺ ions increase the growth rate of Al₂O₃ grain because of the coherency strain energy at grain boundary (Harabi & Davies, 1995; Paek et al., 1996; Riu et al., 2000). However, this

phenomenon is not found in the nanocomposites. It is attributed that the secondary particles of Cr_3C_2 inhibits the growth of alumina matrix. The fracture strength is increased by the grain-boundary modification caused the compressive stress generated by the substitution of bigger Cr^{3+} ion (0.076 nm) in place of smaller Al^{3+} ion (0.068nm). The localized compressive stress helps in strengthening the grain boundary, and then the fracture strength increases by this effect (Lii et al., 1999). The higher toughness of the nanocomposites relative to monolithic alumina may be connected with the stepped transgranular cleavage. The direction of crack propagation within the matrix grains is affected by these dislocations.

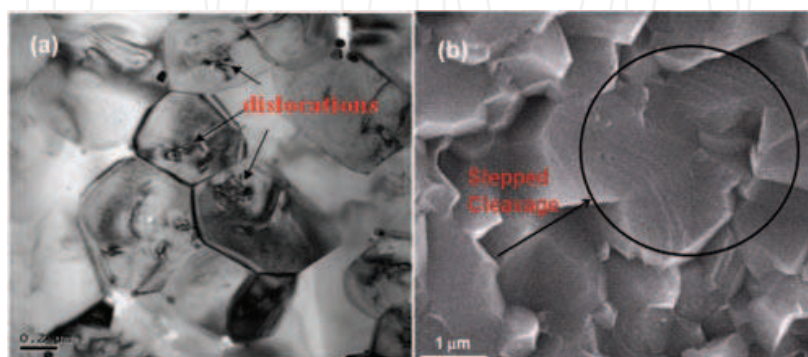


Fig. 17. (a) dislocations and (b) stepped cleavage observed in $\text{Cr}_3\text{C}_2/\text{Al}_2\text{O}_3$ nanocomposites.

4. Densification behavior of $\text{Al}_2\text{O}_3\text{-Cr}_2\text{O}_3/\text{Cr}_3\text{C}_2$ nanocomposites prepared by Spark Plasma Sintering

Compared with conventional hot pressed sintering, spark plasma sintering (SPS) has recently attracted increasing interest due to its ability of rapidly heating the powder compact to high temperatures and consolidating it to high densities within very short time. SPS utilizes applied pressure along with temperature and a pulsed direct current to densify materials. SPS is heralded for its promise in retaining nanostructure features, producing grain boundaries devoid of impurities as well as many other benefits (Kim et al., 2007; Munir et al., 2006; Shen et al., 2002).

As described earlier, the initial powders used for this sintering process were $\text{Al}_2\text{O}_3\text{-Cr}_2\text{O}_3$, which were prepared by metal organic chemical vapor deposition (MOCVD) in a fluidized bed. The nanosized composite powders fabricated in the fluidized bed for 30 and 60 minutes were named as S-30 and S-60, respectively. The pressure of reaction chamber was controlled at 10 torr, and the reaction temperature was kept at 300 °C. The fluidized powders were densified by a SPS process (SPS-515S, Shumitomo, Japan). The 1.5gram of powder (pure Al_2O_3 , S-30, S-60) was put into a graphite mold of 15.5mm diameter. The uniaxial pressure of 50Mpa was imposed on the powder and the vacuum level was less than 6 Pa. The heating rate from room temperature to 600°C and from 600°C to sintering temperature was 200°C/min and 100°C/min, respectively with a holding time of 10 minutes. There were four different sintering temperature conditions of 1200°C, 1250°C, 1300°C and 1350°C conducted in this study.

4.1 Effect of SPS sintering temperature on the color changes of compacts

The color of compacts prepared under different SPS conditions is shown in Fig.18. It is observed that the color of compacts sintered at 1200°C is green; the color of 1250°C compact

is purple; while that of 1300°C and 1350°C are black. Fig. 19 indicates the XRD patterns of the compacts processed by various SPS temperatures. Besides Al_2O_3 peaks, the Cr_2O_3 peaks are found in the compact sintered at 1200°C. Compared with the peak of pure- Al_2O_3 , the Al_2O_3 peaks of compact sintered at higher temperature have slight shifted to lower angles. It means only a little solid-solution of $\text{Al}_2\text{O}_3\text{-Cr}_2\text{O}_3$ has formed in this compact. This result is special to the compacts fabricated by conventional densification methods in which significant pink solid-solution of $\text{Al}_2\text{O}_3\text{-Cr}_2\text{O}_3$ was formed. According to Bondioli et al.,2000, the complete ranges of $\text{Al}_2\text{O}_3\text{-Cr}_2\text{O}_3$ solid solution can be obtained for the reaction temperature higher than 1000°C.

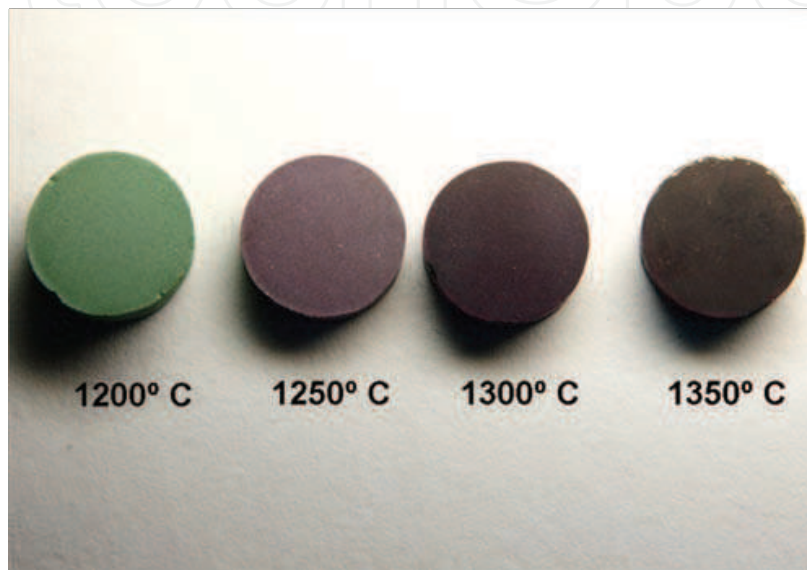


Fig. 18. Optical micrograph of compacts prepared by different SPS temperatures from 1200°C to 1350°C.

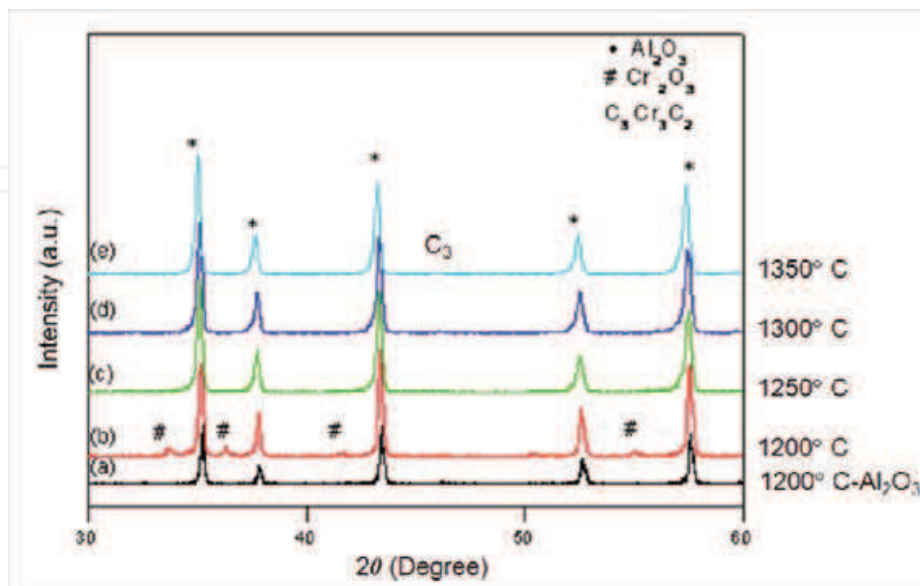
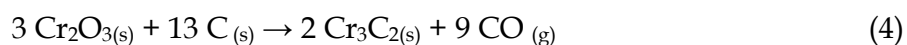


Fig. 19. XRD patterns of (a) pure Al_2O_3 sintered at 1200°C, and the compact at (b) 1200°C, (c) 1250°C, (d) 1300°C and (e) 1350°C for 10 min by SPS.

It is suggested that due to the higher heating rate and short holding time, the most of Cr^{3+} doesn't have enough time to diffuse into Al_2O_3 matrix and remains as Cr_2O_3 phase after the SPS process. The color of pure Cr_2O_3 is green, and so the composite is with green appearance. For the compact sintered at 1250°C , the Cr_2O_3 peaks are disappeared in the XRD pattern because more Cr_2O_3 react with Al_2O_3 matrix to form pinker solid solution in this higher sintering temperature. According to Equation 4 given in (Kubaschewski et al. 1979), chromium carbide would form probably when the temperature is higher than 1150°C . It is believed that there is little black carbide formed when sintered at 1250°C , so the compact exhibits purple color. It is reasonable that the more Cr^{3+} diffuse into Al_2O_3 matrix with the increase in sintering temperature. In comparison to other compacts, more Al_2O_3 peaks of the compact sintered 1350°C have shifted to lower angles observed from XRD patterns. It indicates that more solid solution is formed at a higher temperature. The amount of the solid solution of $\text{Al}_2\text{O}_3\text{-Cr}_2\text{O}_3$ and Cr_3C_2 increases with the increase of sintering temperature.



$$\text{Where, } \Delta G = 261313.95 - 188.5 T \text{ (cal)}$$

The black color of the compact prepared at 1350°C is relevant to the formation of chromium carbide. More Cr_3C_2 is formed as the temperature is over than 1150°C . Cr_3C_2 nanoparticle is observed for the compacts prepared at 1300°C and 1350°C . The TEM diffraction pattern shows the particle with Cr_3C_2 phase as shown in Fig. 20. Although the peak of Cr_3C_2 peaks are not obvious in the XRD patterns in Fig. 19., but based on the Equation 1, sintering at a higher temperature is beneficial to form Cr_3C_2 . In our previous study (Lin et al., 2007), Cr_3C_2 peaks are easy to be found in the XRD patterns as compacts prepared by HP densification in which the vacuum maintained at about 10^{-5} torr, however in this SPS process that is about 6 pa ($\sim 10^{-2}$ torr). According to the report of Chu & Rahmel, 1981, carbon would be consumed by oxygen in a higher oxygen pressure in SPS process and inhibits the formation of Cr_3C_2 .

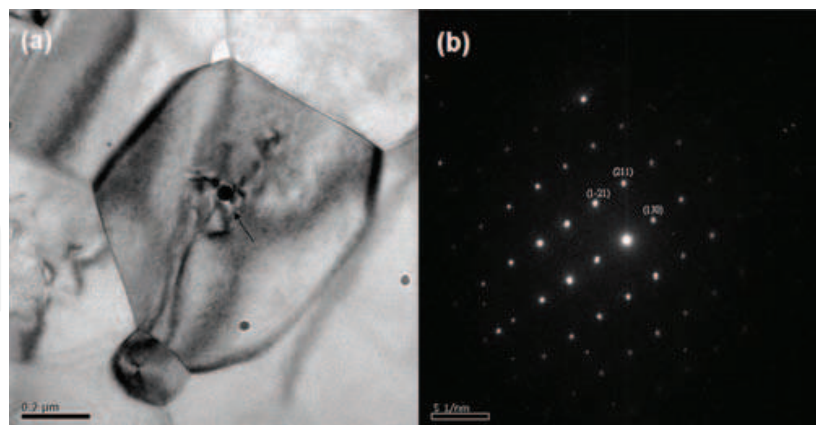


Fig. 20. TEM micrographs of nanocomposites sintered at 1350°C (a) bright field image; (b) SADP of particle in (a).

4.2 Effect of SPS sintering temperature on shrinkage behavior

Fig. 21 shows the sintering shrinkage curves of the pure Al_2O_3 , nanocomposite powders of S-30 and S-60 during the SPS densification in the temperature range $1200^\circ\text{C} \sim 1350^\circ\text{C}$ with holding time of 10 minutes. The y-axis $\Delta L/L_0$ (%) represents the shrinkage profile directly

during densification of the powders in real-time. The trend of Al_2O_3 curve becomes flat at 1200°C , but the curves of S-30 and S-60 still trended up. This means the shrinkage Al_2O_3 has already stopped, but S-30 and S-60 continue shrinking during the period of holding time.

This result is consistent with the apparent density shown in Fig. 22. It shows that pure Al_2O_3 exhibits a higher density than S-30 and S-60, for the sintering temperature at 1200°C and 1250°C . The amount of shrinkage of S-30 is more significant than S-60. The temperature at which the shrinkage vanishes for S-30 and S-60 is 1300°C and 1350°C , respectively as shown in Fig. 21c and 21d. The curves of pure Al_2O_3 , S-30 and S-60 are trended down for the holding temperature at 1350°C . This signifies that all the powder compacts undergone thermal expansion after completion of the sintering shrinkage. The densities of S-30 and S-60 are increased significantly when the temperature rises to 1300°C and 1350°C .

Fig. 21d illustrates that the pure Al_2O_3 starts to densify at about 950°C and finishes at about 1300°C . For S-60 and S-30, the densification temperature starts at about 1050°C and 1100°C , separately, and finishes at 1350°C for both. Actually S-60 finishes its densification after holding about 50 seconds. The second phase particles decrease the diffusivity of grain boundary and lattice, and result in the retardation of densification (Chae et al., 2006). According to XRD spectrum shown in Fig. 19, the delay on the densification process for the nanocomposites is due to the Cr_2O_3 particles coated on Al_2O_3 as sintered at 1200°C . Cr_2O_3 plays as a second phase to inhibit the grain growth during densification. While some of Cr_2O_3 changes to Cr_3C_2 to be the second phase as temperature increases to 1300°C and 1350°C (Lin et al., 2011).

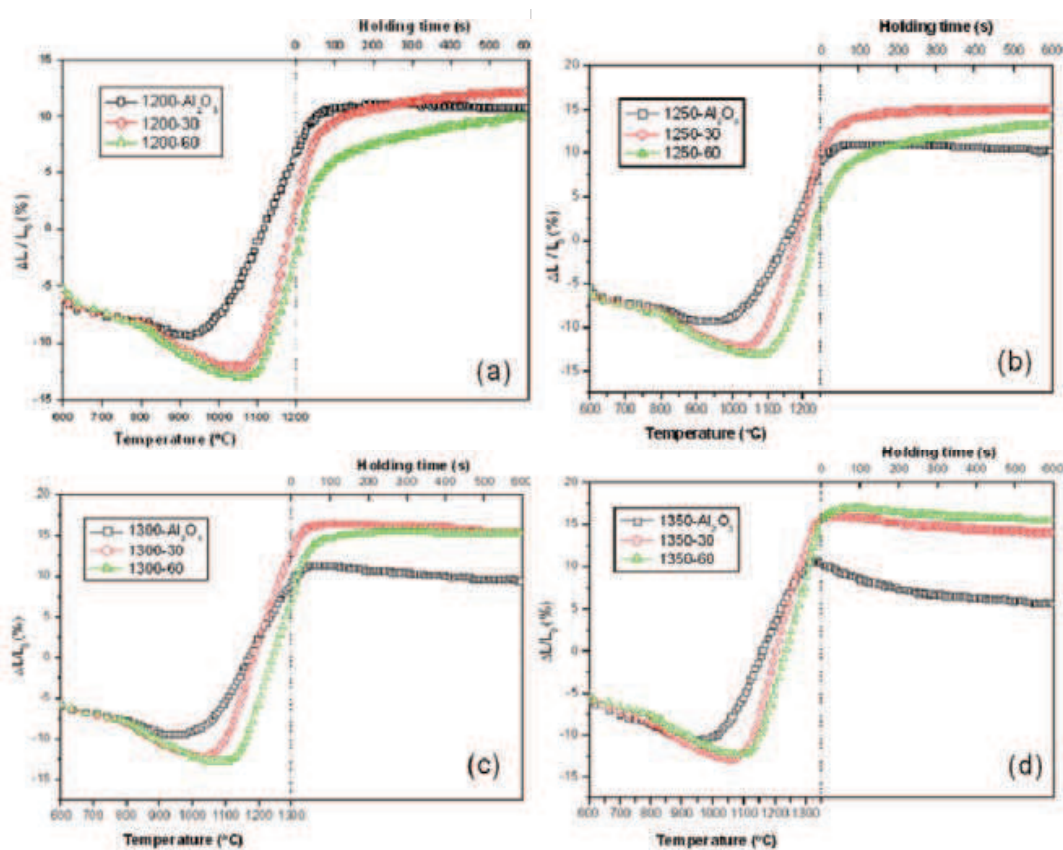


Fig. 21. Sintering shrinkage curves of Al_2O_3 , S-30 and S-60 sintered at (a) 1200°C , (b) 1250°C (c) 1300°C (d) 1350°C for 10 min by SPS.

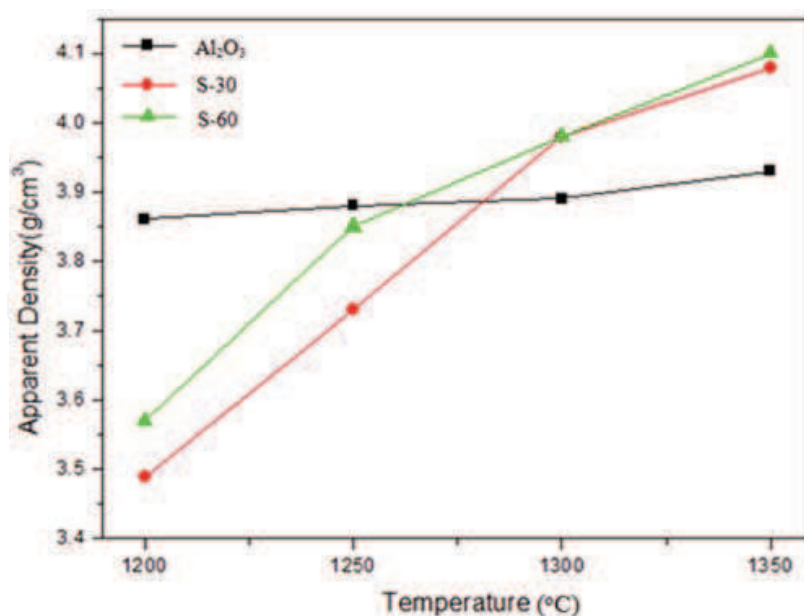


Fig. 22. The apparent density of the specimen of Al₂O₃, S-30, and S-60 prepared at a different SPS sintering temperature from 1200°C to 1350°C.

4.3 Effect of SPS sintering temperature on microstructures and mechanical properties

The fine grains of Al₂O₃-Cr₂O₃/Cr-carbide nanocomposites were prepared by employing spark plasma sintering (SPS) technique. The basic mechanical properties like hardness, fracture strength and toughness were analyzed. The fracture surfaces of the nanocomposites are shown in Fig. 23. It indicates that the pure alumina has larger grain size than that of S-30 and S-60 densification samples. The nanosized reinforced particles (Cr₃C₂) are found in the alumina matrix. S-60 densification sample has smallest grain size due the more amounts of secondary phase particles to inhibit its grain growth. The hardness, fracture strength and toughness of the S-30 and S-60 nanocomposites are present in Fig. 24. The S-60 nanocomposite exhibits highest fracture strength and toughness. The increase in hardness, fracture strength and toughness of nanocomposites over monolithic alumina is due to the strengthening of secondary phase of Cr₃C₂ particles and solid solution of Al₂O₃-Cr₂O₃. The co-relation between the microstructure and mechanical properties is similar to that of nanocomposites prepared using hot press sintering described in section 3.3.

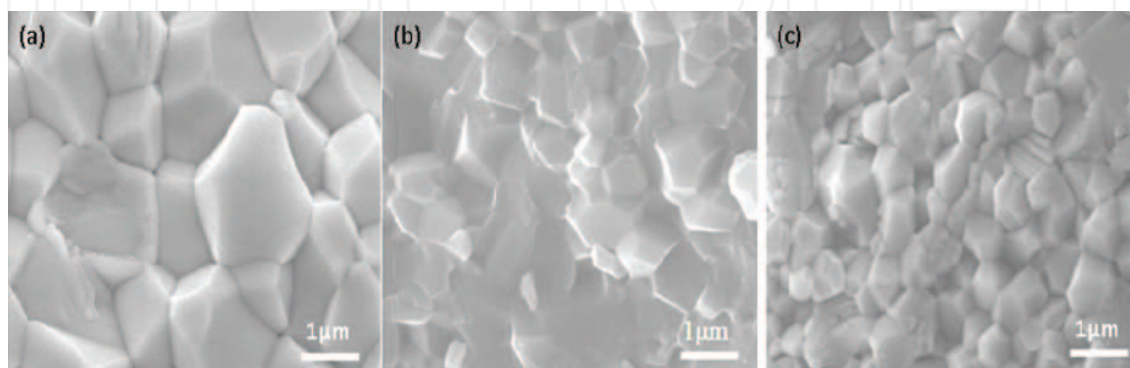


Fig. 23. SEM micrographs of fracture surface of 1350°C fully dense SPS specimen of (a) Al₂O₃, (b) S-30, (c) S-60.

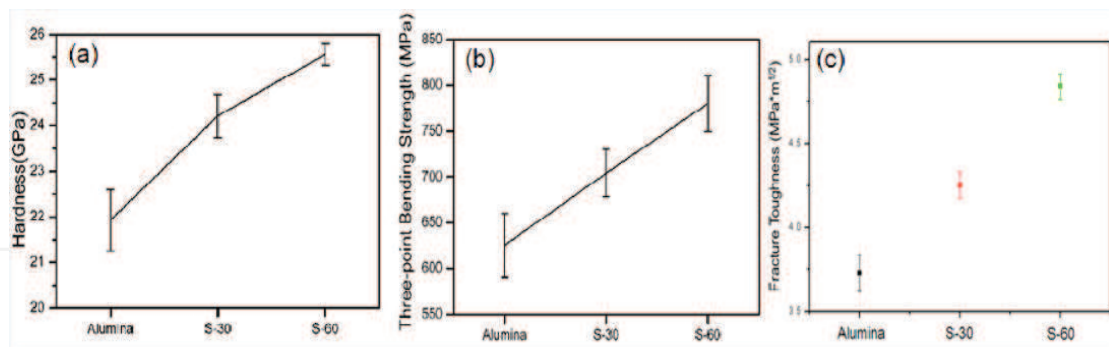


Fig. 24. (a) Hardness, (b) Fracture Strength and (c) Toughness of Chromium Carbide/Alumina nanocomposites sintered at 1350°C for 10min by SPS.

5. Conclusion

Nanoscaled Cr_2O_3 powder with an average particle size of 20–40 nm, coated on alumina particles, has been produced by means of chemical vapor deposition in a fluidized chamber, using the pyrolysis of $\text{Cr}(\text{CO})_6$ precursor. The pyrolysis of $\text{Cr}(\text{CO})_6$ at 300 and 400 °C produces amorphous and crystalline Cr_2O_3 particles, respectively. The decomposed precursor consists of Cr_2O_3 , Cr_{1-x} and C. To prepare nanoscaled chromium carbide powder from the nanometer-sized Cr_2O_3 , carbonizing behavior of the Cr_2O_3 particles was investigated using a graphite furnace at 1150 °C. It was found that, when amorphous Cr_2O_3 powders were carbonized at 1150 °C, the powder was transformed into Cr_3C_2 , while the crystalline Cr_2O_3 was transformed into a mixture of Cr_7C_3 and Cr_3C_2 . These transformations were confirmed by X-ray diffraction (XRD), transmission electron microscopy (TEM), and energy dispersive spectroscopy (EDS). A solid solution of Al_2O_3 - Cr_2O_3 and an Al_2O_3 - Cr_2O_3 / Cr_3C_2 nanocomposite were formed when these fluidized powders were pre-sintered at 1000 and 1150 °C, respectively before hot-pressing at 1400 °C. In addition, an Al_2O_3 - Cr_2O_3 / Cr -carbide (Cr_3C_2 and Cr_7C_3) nanocomposite was formed when the particles were directly hot pressed at 1400 °C.

The undesirable solid solution leads to abnormal grain growth of the Al_2O_3 matrix and decreases the desired Cr_3C_2 contents in the composite. In order to avoid this drawback, carbothermal reduction process was adopted using methane as the carbonization source. The carburization process involved the sequential deposition of carbon on the outer surface of the Cr_2O_3 powder followed by carbon diffusion into the powder, leading to the formation of metastable $\text{Cr}_3\text{C}_{2-x}$ phase and stable Cr_3C_2 in the temperature range 700–850 °C. The phase transformation from Cr_2O_3 to Cr_3C_2 has been characterized by XRD, X-ray photoelectron spectroscopy (XPS) and electron energy loss spectroscopy (EELS). It is observed that the formation of carbon nanofilms surrounding the carbide crystallites provides the stress and assists the phase transformation from metastable $\text{Cr}_3\text{C}_{2-x}$ to stable Cr_3C_2 .

The densification behavior of Al_2O_3 - Cr_2O_3 / Cr_3C_2 nanocomposites has been studied using the recently developed SPS technique. Different colors of the compacts such as green, purple and black were observed during densification process at different SPS temperatures from 1200 °C to 1350 °C. These changes in color were relevant to the existence of secondary phase of green Cr_2O_3 , pink solid solution of Al_2O_3 - Cr_2O_3 and black Cr_3C_2 at different SPS temperature. This SPS process reduces the abnormal grain growth of Al_2O_3 , which appears

during hot press sintering and $\text{Al}_2\text{O}_3\text{-Cr}_2\text{O}_3/\text{Cr}_3\text{C}_2$ nanocomposites exhibit small grain size in this process. The microstructure and basic mechanical properties such as hardness, fracture strength and toughness of pure alumina as well as this nanocomposite have been analyzed. The microstructure of dislocation, transgranular and step-wise fracture surface were observed in the nanocomposites. The nanocomposites show fracture strength (780MPa) and fracture toughness ($4.8 \text{ Mpa}\cdot\text{m}^{1/2}$), which is higher than monolithic alumina. In comparison with monolithic alumina, the $\text{Al}_2\text{O}_3\text{-Cr}_2\text{O}_3/\text{Cr}_3\text{C}_2$ nanocomposites exhibit higher hardness, fracture strength and toughness due to the strengthening of secondary phase of Cr_3C_2 particles and solid solution of $\text{Al}_2\text{O}_3\text{-Cr}_2\text{O}_3$.

6. Acknowledgment

Authors are thankful to National Science Council of Taiwan for its financial support under the contract No: 99-2923-E-006- 002-MY3 to carryout the present work.

7. References

- Anya, C. C. (1999). Microstructural nature of strengthening and toughening in $\text{Al}_2\text{O}_3\text{-SiC}(p)$ nanocomposites. *Journal of Materials Science*, Vol. 34, No. 22, pp. 5557-5567, ISSN 0022-2461
- Awaji, H.; Choi, S.-M. & Yagi, E. (2002). Mechanisms of toughening and strengthening in ceramic-based nanocomposites, *Mechanics of Materials*, Vol. 34, pp. 411-422, ISSN 0167-6636
- Anacleto, N. & Ostrovski, O. (2004). Solid-state reduction of chromium oxide by methane-containing gas. *Metallurgical and Materials Transactions B*, Vol. 35, No. 4, pp. 609-615, ISSN 1073-5615
- Arévalo-López, A. M. & Alario-Franco, M. A. (2009). Reliable method for determining the oxidation state in chromium oxides. *Inorganic Chemistry*, Vol. 48, pp. 11843-11846, ISSN 0020-1669
- Bradt, R. C. (1967). Cr_2O_3 solid solution hardening of Al_2O_3 . *Journal of the American Ceramic Society*, Vol. 50, No. 1, (January 1967), pp. 54-55, ISSN 1551-2916
- Bewilogua, K.; Heinitz, H.-J., Rau, B. & Schulze, S. (1988). A chromium carbide phase with B1 structure in thin film prepared by ion plating. *Thin Solid Films*, Vol. 167, No. 1-2, (December 1988), pp. 233-243, ISSN 0040-6090
- Becher, P. F. (1991). Microstructural design of toughened ceramics. *Journal of the American Ceramic Society*, Vol. 74, No. 2, (February 1991), pp. 255-269, ISSN 1551-2916
- Bouzy, E.; Bauer-Grosse, E. & Le Caër, G. (1993). NaCl and filled Re_3B -type structures for two metastable chromium carbides. *Philosophical Magazine B*, Vol. 68, No. 5, pp. 619-638, ISSN 0958-6644
- Borsa, C. E. & Brook, R. J. (1995). Fabrication of $\text{Al}_2\text{O}_3/\text{SiC}$ nanocomposites using a polymeric precursor for SiC. In *Ceramic Transactions Vol. 51, Ceramic Processing and Science*, The American Ceramic Society, H. Hausner, G. L. Messing and S.-I. Hirano, (Ed.), 653-657, Westerville, OH
- Borsa, C. E.; Ferreira, H. S. & Kiminami, R. H. G. A. (1999). Liquid Phase Sintering of $\text{Al}_2\text{O}_3/\text{SiC}$ Nanocomposites. *Journal of the European Ceramic Society*, Vol. 19, No. 5, (May 1999), pp. 615-621, ISSN 0955-2219

- Bondioli, F.; Ferrari, A. M., Leonelli, C. & Manfredini, T. J. (2000). Reaction mechanism in alumina/chromia($\text{Al}_2\text{O}_3\text{-Cr}_2\text{O}_3$) solid solutions obtained by coprecipitation. *Journal of the American Ceramic Society*, Vol. 83, No.8, (August 2000) pp. 2036–2040, ISSN 1551-2916
- Berger, L.-M.; Stole, S. Gruner, W. & Wetzig, K. (2001). Investigation of the carbothermal reduction process of chromium oxide by micro- and lab-scale methods. *International Journal of Refractory Metals and Hard Materials*, Vol. 19, No. 2, (March 2001), pp. 109–121, ISSN 0263-4368
- Chu, W. F. & Rahmel, A. (1981). The Conversion of Chromium Oxide to Chromium Carbide. *Oxidation of Metals*, Vol. 15, pp. 331-337, ISSN 1573-4889
- Chou, Y. S. & Green D. J. (1992). Silicon carbide platelet/alumina composites: I, Effect of forming technique on platelet orientation. *Journal of the American Ceramic Society*, Vol. 75, No. 12, (December 1992), pp. 3346-3352, ISSN 1551-2916
- Carroll, L.; Sternitzke, M. & Derby, B. (1996). Silicon carbide particle size effects in alumina based nanocomposites. *Acta Materialia*, Vol. 44, No. 11, (November 1996), pp. 4543-4552, ISSN 1359-6454
- Chen, C. L. & Wei, W. C. J. (2002). Sintering behavior and mechanical properties of nano-sized $\text{Cr}_3\text{C}_2/\text{Al}_2\text{O}_3$ composites prepared by MOCVI process. *Journal of the European Ceramic Society*, Vol. 22, No.16, (December 2002), pp. 2883-2892, ISSN 0955-2219
- Choi, S. M.; Honda, S., Nishikawa, T., Awaji, H., Gnanam, F. D., Vishista, K. & Kuroyama, T. (2004). Design concept of strengthening and toughening mechanisms in nanocomposites—ceramic metal nanocomposites. *Journal of the Ceramic Society of Japan*, Vol. 112, pp. S912–S915, ISSN 0914-5400
- Choi, S. M. & Awaji, H. (2005). Nanocomposites-a new material design concept. *Science and Technology of Advanced Materials*, Vol. 6, pp. 2-10, ISSN 1468-6996
- Chae, J. H.; Kim, K. H. Choa, Y. H. Matsushita, J. I. Yoon, J. W. & Shim, K. B. (2006). Microstructural Evolution of $\text{Al}_2\text{O}_3\text{-SiC}$ Nanocomposites During Spark Plasma Sintering. *Journal of Alloys and Compounds*, Vol. 413, pp. 259-264, ISSN 0925-8388
- Davidge, R. W. (1979). *Mechanical behaviour of ceramics*, Cambridge Solid State Science Series, ISBN : 978-0521293099, Cambridge University Press
- Daulton, T. L.; Little, B. J. Lowe, K. & Jones-Meehan, J. (2002). Electron energy loss spectroscopy techniques for the study of microbial chromium(VI) reduction. *Journal of Microbiological Methods*, Vol. 50, pp.39-54, ISSN 0167-7012
- Dusza, J.; Blugan, G., Morgiel, J., Kuebler, J., Inam, F., Peijs, T., Reece, M. J. & Puchy V. (2009). Hot pressed and spark plasma sintered zirconia/carbon nanofiber composites, *Journal of the European Ceramic Society*, Vol. 29, No. 15, (December 2009), pp. 3177–3184, ISSN 0955-2219
- Fu, C. T.; Wu, J. M. & Li, A. K. (1994). Microstructure and mechanical properties of Cr_3C_2 particulate reinforced Al_2O_3 matrix composites. *Journal of Materials Science*, Vol. 29, No.10, pp. 2671-2677, ISSN 0022-2461
- Fan, X.; Dickey, E. C., Pennycook, S. J. & Sunkara, M. K. (1999). Z-contrast imaging and electron energy-loss spectroscopy analysis of chromium-doped diamond-like carbon films. *Applied physics letters*, Vol. 75, pp. 2740-2742, ISSN 0003-6951
- Ghate, B. B.; Smith, W. C., Kim, C., Hasselman, D. P. H. & Kane, G. E. (1975). Effect of chromia alloying on machining performance of alumina ceramic cutting tools.

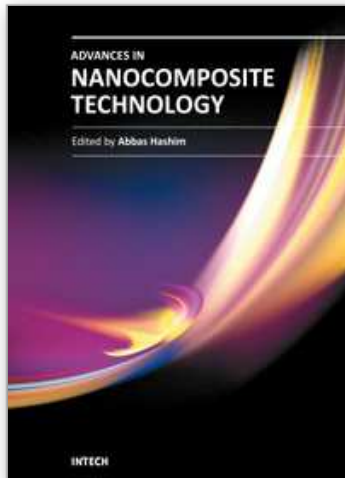
- American Ceramic Society Bulletin, Vol. 54, No.2, (February 1975), pp. 210-215, ISSN 0002-7812
- Galusek, D.; Sedláček, J., Švančárek, P., Riedel, R., Satet, R. & Hoffmann, M. (2007). The influence of post-sintering HIP on the microstructure, hardness, and indentation fracture toughness of polymer-derived Al₂O₃-SiC nanocomposites. *Journal of the European Ceramic Society*, Vol. 27, No. 2-3, pp. 1237-1245, ISSN 0955-2219
- Harabi, A. & Davies, T. J. (1995). Densification and grain growth in sintered alumina-chromia powder mixtures. *British Ceramic Transactions*, Vol. 94, pp. 97-102, ISSN 0967-9782
- Han, S. C.; Yoon, D. Y. & Brun, M. K. (1995). Migration of grain boundaries in alumina induced by chromia addition. *Acta Metallurgica et Materialia*, Vol. 43, No.3, (March 1995), pp. 977-984, ISSN 1359-6454
- Huang, J. L.; Lin, H. D. Jeng, C. A. & Lii, D. F. (2000). Crack growth resistance of Cr₃C₂/Al₂O₃ composites. *Material science and Engineering A*, Vol. 279, No. 1-2, (February 2000), pp. 81-86, ISSN 0921-5093
- Inoue, A. & Masumoto, T. (1979). Formation of Nonequilibrium Cr₃C Carbide in Cr-C Binary Alloys Quenched Rapidly From the Melt. *Scr. Metall.*, Vol. 13, pp. 711-715, ISSN 1359-6462
- Kunii, D. & Levenspiel, O. (1977). *Fluidization Engineering*, pp. 195-223, ISBN 10:0-409-90233-0, Hunting-ton, NY, ISBN 10: 0-409-90233-0
- Kubaschewski, O. & Alcock, C. B. (1979). *Metallurgical thermochemistry, 5th ed.* ISBN 9780080208978, Netherlands
- Kim, B. N.; Hirga, K. Morita, K. & Yoshida, H. (2007). Spark Plasma Sintering of Transparent Alumina, *Scripta Materialia*, Vol. 57, pp. 607-610, ISSN 1359-6462
- Kumari, L.; Zhang, T., Du, G. H., Li, W. Z., Wang, Q. W., Datsy, A. & Wu, K. H. (2009). Synthesis, microstructure and electrical conductivity of carbon nanotube-alumina nanocomposites. *Ceramics International*, Vol. 35, No. 5, (July 2009), pp. 1775-1781, ISSN 0272-8842
- Lander, J. J. & Germer, L. H. (1947). Plating molybdenum, tungsten, and chromium by thermal decomposition of their carbonyls. *Am. Inst. Min. Metal. Eng. Tech.*, Vol. 14, No. 6, pp. 1-42
- Lange, F. F. (1973). Effect of microstructure on strength of Si₃N₄-SiC composite system. *Journal of the American Ceramic Society*, Vol. 56, No. 9, (September 1973), pp. 445-450, ISSN 1551-2916
- Lange, F. F. (1989). Powder processing science and technology for increased reliability. *Journal of the American Ceramic Society*, Vol. 72, No.1, (January 1989), pp. 3-15, ISSN 1551-2916
- Lio, S.; Watanabe, M., Matsubara, M. & Matsuo, Y. (1989). Mechanical properties of alumina/silicon carbide whisker composites. *Journal of the American Ceramic Society*, Vol. 72, No. 10, (October 1989), pp. 1880-1884, ISSN 1551-2916
- Lozzi, L.; Passacantando, M. Picozzi, P. Santucci, S. & Crescenzi, M. D. (1991). Electronic structure of Cr clusters on graphite. *Atoms, Molecules and Cluster*, Vol. 20, pp. 387-390.
- Lerch, A. & Rousset, A. (1994). Influence of morphology on textural properties and on the reactivity of chromium oxides obtained by decomposition of oxalate precursors

- (NH₄)₃[Cr(C₂O₄)₃]. *Thermochimica Acta*, Vol. 232, No. 2, (February 1994), pp. 233-242, ISSN 0040-6031
- Levin, I.; Kaplan, W. D. Brandon, D. G. & Layous, A. (1995). Effect of SiC Submicrometer Particle Size Content on Fracture Toughness of Alumina-SiC " Nanocomposites". *Journal of the American Ceramic Society*, Vol.78, No. 1, pp. 254-256, ISSN 1551-2916
- Loubière, S.; Laurent, Ch., Bonino, J. P.& Rousset, A.(1995). Elaboration, Microstructure and Reactivity of Cr₃C₂ powders of different morphology. *Materials Research Bulletin*, Vol. 30, pp. 1535-1546, ISSN 0025-5408
- Loubière, S.; Laurent, Ch., Bonino, J. P.& Rousset, A. (1996). A metastable chromium carbide powder obtained by carburization of a metastable chromium oxide. *Journal of Alloys and Compounds*, Vol. 243, pp. 59-66, ISSN 0925-8388
- Lii, D. F.; Huang, J. L. Huang, J. J. & Lu, H. H. (1999). The interfacial reaction in Cr₃C₂/Al₂O₃ composites. *Journal of Materials Research*, Vol. 14, No.3, (March 1999), pp. 817-823, ISSN 0884-2914
- Lii, C. L.; Riu, D. H., Sekino, T. & Niihara, K. (1999). Fabrication and Mechanical Properties of Al₂O₃ Solid Solution with low addition of Cr₂O₃. *Key Engineering Materials*, Vols. 161-163, pp. 161-164, ISSN 1662-9795
- Liu, X. K.; Zhu, D. M. & Hou, W. C. (2006). Microwave permittivity of SiC-Al₂O₃ composite powder prepared by sol-gel and carbothermal reduction. *Transactions of Nonferrous Metals Society of China*, Vol. 16, pp. s494-s497, ISSN 1003-6326
- Lin, H. T.; Huang, J. L., Lo, W. T. & Wei, W. C. J. (2005). Investigation on carbonizing behaviors of nanometer-sized Cr₂O₃ particles dispersed on alumina particles by MOCVD in fluidized bed. *Journal of Material Research*, Vol. 20, No. 8, (August 2005), pp. 2154-2160, ISSN 0884-2914
- Lin, H. T.; Huang, W. S. Wang, S. C. Lu, H. H. Wei, W. C. J. & Huang, J. L. (2006). Investigation of chromium carbide/alumina nano-composite prepared via MOCVD in fluidized bed and densification process. *Materials Science and Engineering B*, Vol. 127, No. 1, (February 2006), pp. 22-28, ISSN 0921-5107
- Lin, H. T.; Huang, J. L. Wang, S. C. & Lin, C. F. (2006). Preparation of nano-scale Cr₃C₂ particles dispersed on alumina particles by MOCVD in fluidized reactor and carbothermal treatment. *Journal of Alloys and Compounds*, Vol. 417, No. 1-2, (June 2006), pp. 214-219, ISSN 0925-8388
- Lin, H. T.; Huang, J. L. & Wang, S. C. (2007). Investigation of Hot-Pressed Al₂O₃-Cr₂O₃/Cr₃C₂ Nanocomposite, *Key Engineering Materials*, Vol. 351, pp. 93-97, ISSN 1662-9795
- Lin, H. T.; Wang, S. C., Huang, J. L. & Chang, S. Y.(2007).Processing of Hot Pressed Al₂O₃-Cr₂O₃/Cr-carbide Nanocomposite Prepared by MOCVD in a Fluidized Bed. *Journal of the European Ceramic Society*, Vol. 27, pp. 4759-4765, ISSN 0955-2219
- Lin, H. T.; Nayak, P. K. Wang, S. C. Chang, S.Y. & Huang, J. L. (2011) Electron-energy loss spectroscopy and Raman studies of nanosized chromium carbide synthesized during carbothermal reduction process from precursor Cr(CO)₆. *Journal of the European Ceramic Society*, Article in Press, ISSN 0955-2219
- Lin, H. T.; Liu, B. Z. Shio, C. W. & Huang, J. L. (2011). Study of color change in Al₂O₃-Cr₂O₃/Cr₃C₂ Nanocomposites prepared by Spark Plasma Sintering, *Ceramics Internationals*, In Press, ISSN 0272-8842

- Muradov, N. Z. (1998). CO₂-Free Production of Hydrogen by Catalytic Pyrolysis of Hydrocarbon Fuel. *Energy & Fuels*, Vol. 12, pp. 41-48, ISSN 0887-0624
- Muradov, N. Z. (2001). Hydrogen via methane decomposition: an application for decarbonization of fossil fuels, *International Journal of Hydrogen Energy*, Vol. 26, pp. 1165-1175, ISSN 0360-3199
- Munir, Z. A.; Anselmi-Tamburini, U. & Ohyanagi, M.(2006).The Effect of Electric Field and Pressure on the Synthesis and Consolidation of Materials: A Review of the Spark Plasma Sintering Method. *Journal of Materials Science*, Vol. 41,pp. 763-777, ISSN 0022-2461
- Nassau, K.(1983). *The Physics and Chemistry of Color*. Wiley, New York, pp. 77-106
- Niihara, K. & Hirai, T. (1986). Super-Fine Microstructure and Toughness of Ceramics. *Bull. Cerum. Soc. Jpn.*, Vol. 21, No. 7, pp.598-604
- Niihara, K & Nakahira, A. (1988). Strengthening of oxide ceramics by SiC and Si₃N₄ dispersions. In: *Proceedings of the Third International Symposium on Ceramic Materials and Components for Engines*, The American Ceramic Society, V. J. Tennery, (Ed.), 919-926, Westerville, Ohio
- Niihara, K.; Nakahira, A., Sasaki, G. & Hirabayashi, M. (1989). Development of strong Al₂O₃/SiC composites, *Proceedings of the First MRS International Meeting on Advanced Materials*, ISBN 1558990305, Sunshine City, Ikebukuro, Tokyo, Japan, May-June, 1988, Vol. 4, pp. 129-134, ISBN 1558990305
- Niihara, K. (1991). New design concept for structural ceramics-Ceamic nanocomposites. *The Centennial Memorial Issue of The Ceramic Society of Japan*, Vol. 99, No. 10, pp. 974-982, ISSN 0914-5400
- Ohji, T.; Jeong, Y-K., Choa, Y-H. & Niihara, K. (1998). Strengthening and toughening mechanisms of ceramic nanocomposites, *Journal of the European Ceramic Society*, Vol. 81, No. 6, (June 1988), pp.1453-1460, ISSN 0955-2219
- Paek, Y. K.; Lee, H. Y. & Kang, S. -J. L. (1996). Direction of liquid film migration induced by chromic oxide in alumina-anorthite. *Journal of the American Ceramic Society*, Vol. 79, pp. 3029-3032, ISSN 1551-2916
- Riu, D. H.; Kong, Y. M., & Kim, H. E. (2000). Effect of Cr₂O₃ addition on microstructural evolution and mechanical properties of Al₂O₃. *Journal of the European Ceramic Society*, Vol. 20, pp.1475-1481, ISSN 0955-2219
- Storms, Edmund K.(1967). *The Refractory Carbides*. Refractory Materials, Vol. 2, New York, Academic Press, pp. 247-268
- Sigl, L. S.; Mataga, P. A., Dalgleish, B. J., McMeeking, R. M. & Evans, A. G.(1988). On the toughness of brittle materials reinforced with a ductile phase. *Acta Metallurgica*, Vol. 36, No. 4, (April 1988), pp. 945-953, ISSN 1359-6454
- Sekino, T. & Niihara, K. (1997). Fabrication and mechanical properties of fine-tungsten-dispersed alumina-based composites, *Journal of Materials Science*, Vol. 32, No. 15, (November 1997), pp. 3943-3949, ISSN 0022-2461
- Sternitzke, M. (1997). Review: structural ceramic nanocomposites, *Journal of the European Ceramic Society*, Vol. 17, No.9, pp. 1061-1082, ISSN 0955-2219
- Shen, Z.; Johnsson, M. Zhao, Z. & Nygren, M. (2002). Spark Plasma Sintering of Alumina. *Journal of the American Ceramic Society*, Vol. 85, pp. 1921-1927, ISSN 1551-2916
- Shapiro, I. P.; Todd, R. I., Titchmarsh, J. M. & Roberts, S.G.(2009). Effects of Y₂O₃ additives and powder purity on the densification and grain boundary composition of

- Al₂O₃/SiC nanocomposites. *Journal of the European Ceramic Society*, Vol. 29, NO. 9, (June 2009), pp. 1613–1624, ISSN 0955-2219
- Tsugeki, K.; Kato, T., Koyanagi, Y., Kusakabe, K. & Morooka, S. (1993). Electro conductivity of sintered bodies of α -Al₂O₃-TiN composite prepared by CVD reaction in a fluidized bed. *Journal of Materials Science*, Vol. 28, No. 12, pp. 3168-3172, ISSN 0022-2461
- Trombini, V.; Pallone, E. M. J. A., Tamburini, U. A., Munir, Z. A. & Tomasi, R. (2009). Characterization of alumina matrix nanocomposite with ZrO₂ inclusions densified by spark plasma sintering, *Materials Science and Engineering: A*, Vol. 501, No. 1-2, (February 2009), pp. 26-29, ISSN 0921-5093
- Vollath, D. & Sickafus K. E. (1992). Synthesis of nanosized ceramic oxide powders by microwave plasma reactions. *Nanostructured Materials*, Vol. 1, No.5, (September-October 1992), pp. 427-437
- Vollath, D. & Sickafus, K. E. (1993). Synthesis of nanosized ceramic nitride powders by microwave supported plasma reactions. *Nanostructured Materials*, Vol. 2, No. 5, (September-October 1993), pp. 451-456
- Vollath, D.; Szabó D. V. & HauBelt, J. (1997). Synthesis and Properties of Ceramic Nanoparticles and Nanocomposites, *Journal of the European Ceramic Society*, Vol. 17, No. 11, pp. 1317-1324, ISSN 0955-2219
- Vollath, D. & Szabó, D. V. (2006). Microwave Plasma Synthesis of Ceramic Powders, In: *Advances in Microwave and Radio Frequency Processing*, Part-IX, pp. 619-626, Springer
- Wagner, C. D.; Riggs, W. M., Davis, L. E., Moulder, J. F. & Muilenberg, G. E. (1979). *Handbook of X-ray Photoelectron Spectroscopy*, Perkin-Elmer Corp., Minnesota, USA
- Wang, Y. & Hsu, S. M. (1996). The effects of operating parameters and environment on the wear and wear transition of alumina. *Wear*, Vol. 195, No. 1-2, (July 1996), pp. 90-99, ISSN 0043-1648
- Wang, S. C.; Lin, H. T. Nayak, P. K. Chang, S. Y. & Huang, J. L. (2010). Carbothermal reduction process for synthesis of nanosized chromium carbide via metal-organic vapor deposition. *Thin Solid Films*, Vol. 518, pp. 7360–7365, ISSN 0040-6090
- Xu, Y.; Nakahira, A. & Niihara, K. (1994). Characteristics of Al₂O₃-SiC nanocomposite prepared by sol-gel processing. *Journal of the Ceramic Society of Japan*, Vol. 102, No. 3, pp. 312-315, ISSN 0914-5400

IntechOpen



Advances in Nanocomposite Technology

Edited by Dr. Abbass Hashim

ISBN 978-953-307-347-7

Hard cover, 374 pages

Publisher InTech

Published online 27, July, 2011

Published in print edition July, 2011

The book “Advances in Nanocomposite Technology” contains 16 chapters divided in three sections. Section one, “Electronic Applications”, deals with the preparation and characterization of nanocomposite materials for electronic applications and studies. In section two, “Material Nanocomposites”, the advanced research of polymer nanocomposite material and polymer-clay, ceramic, silicate glass-based nanocomposite and the functionality of graphene nanocomposites is presented. The “Human and Bioapplications” section is describing how nanostructures are synthesized and draw attention on wide variety of nanostructures available for biological research and treatment applications. We believe that this book offers broad examples of existing developments in nanocomposite technology research and an excellent introduction to nanoelectronics, nanomaterial applications and bionanocomposites.

How to reference

In order to correctly reference this scholarly work, feel free to copy and paste the following:

Jow-Lay Huang and Pramoda Nayak (2011). Processing and Characterization of Alumina/ Chromium Carbide Ceramic Nanocomposite, Advances in Nanocomposite Technology, Dr. Abbass Hashim (Ed.), ISBN: 978-953-307-347-7, InTech, Available from: <http://www.intechopen.com/books/advances-in-nanocomposite-technology/processing-and-characterization-of-alumina-chromium-carbide-ceramic-nanocomposite>

INTECH
open science | open minds

InTech Europe

University Campus STeP Ri
Slavka Krautzeka 83/A
51000 Rijeka, Croatia
Phone: +385 (51) 770 447
Fax: +385 (51) 686 166
www.intechopen.com

InTech China

Unit 405, Office Block, Hotel Equatorial Shanghai
No.65, Yan An Road (West), Shanghai, 200040, China
中国上海市延安西路65号上海国际贵都大饭店办公楼405单元
Phone: +86-21-62489820
Fax: +86-21-62489821

© 2011 The Author(s). Licensee IntechOpen. This chapter is distributed under the terms of the [Creative Commons Attribution-NonCommercial-ShareAlike-3.0 License](#), which permits use, distribution and reproduction for non-commercial purposes, provided the original is properly cited and derivative works building on this content are distributed under the same license.

IntechOpen

IntechOpen